JGR Space Physics

RESEARCH ARTICLE
10.1029/2018JA026453

# Dynamical Coupling Between Hurricane Matthew and the Middle to Upper Atmosphere via Gravity Waves

**Shuang Xu[1], Jia Yue[2], Xianghui Xue[1], Sharon L. Vadas[3], Steven D. Miller[4], Irfan Azeem[5], William Straka III[6], Lars Hoffmann[7], and Simin Zhang[8]**

[1]School of Earth and Space Sciences, University of Science and Technology of China, Hefei, China, [2]Department of Atmospheric and Planetary Sciences, Hampton University, Hampton, VA, USA, [3]Northwest Research Associates, Boulder, CO, USA, [4]Cooperative Institute for Research in the Atmosphere, Colorado State University, Fort Collins, CO, USA, [5]ASTRA LLC, Boulder, CO, USA, [6]Cooperative Institute for Meteorological Satellite Studies, University of Wisconsin Madison, Madison, WI, USA, [7]Jülich Supercomputing Centre, Forschungszentrum Jülich, Jülich, Germany, [8]Key Laboratory of High Power Laser and Physics, Shanghai Institute of Optics and Fine Mechanics, Chinese Academy of Sciences, Shanghai, China

**Key Points:**
- Concentric gravity waves generated by Hurricane Matthew were seen from the tropopause to the ionosphere on October 2016
- These concentric gravity waves had horizontal wavelengths of ~200–350 km
- Small and large concentric gravity waves observed in airglow layer and ionosphere correlated with Hurricane Matthew's strongest period

**Correspondence to:**
S. Xu,
xush9@mail.ustc.edu.cn

**Citation:**
Xu, S., Yue, J., Xue, X., Vadas, S. L., Miller, S. D., Azeem, I., et al. (2019). Dynamical coupling between Hurricane Matthew and the middle to upper atmosphere via gravity waves. *Journal of Geophysical Research: Space Physics*, *124*, 3589–3608. https://doi.org/10.1029/2018JA026453

Received 28 DEC 2018
Accepted 2 APR 2019
Accepted article online 15 APR 2019
Published online 13 MAY 2019



**Abstract** During 30 September to 9 October 2016, Hurricane Matthew traversed the Caribbean Sea to the east coast of the United States. During its period of greatest intensity, in the central Caribbean, Matthew excited a large number of concentric gravity waves (GWs or CGWs). In this paper, we report on hurricane-generated CGWs observed in both the stratosphere and mesosphere from spaceborne satellites and in the ionosphere by ground Global Positioning System receivers. We found CGWs with horizontal wavelengths of ~200–300 km in the stratosphere (height of ~30–40 km) and in the airglow layer of the mesopause (height of ~85–90 km), and we found concentric traveling ionospheric disturbances (TIDs or CTIDs) with horizontal wavelengths of ~250–350 km in the ionosphere (height of ~100–400 km). The observed TIDs lasted for more than several hours on 1, 2, and 7 October 2016. We also briefly discuss the vertical and horizontal propagation of the Hurricane Matthew-induced GWs and TIDs. This study shows that Hurricane Matthew induced significant dynamical coupling between the troposphere and the entire middle and upper atmosphere via GWs. It is the first comprehensive satellite analysis of gravity wave propagation generated by hurricane event from the troposphere through the stratosphere and mesosphere into the ionosphere.

## 1. Introduction

A tropical cyclone (TC) is a nonfrontal rotating low-pressure weather system with organized convective bands and strong, sustained surface winds. A hurricane is a strong TC with maximum sustained winds over 74 miles per hour (mph, ~119 km/hr) originating in the central North Pacific, eastern North Pacific, and North Atlantic (including the Caribbean Sea and the Gulf of Mexico) basins. Typhoons are TCs that occur in the Northwest Pacific. In the South Pacific and Indian Ocean, the generic term of TC is used. Each year, the hurricane season in the North Atlantic starts on 1 June and ends on 30 November. On average, there are 12.1 tropical storm or stronger (greater than 17 m/s sustained winds) and 6.4 hurricane/severe TC (greater than 33 m/s sustained winds) per year from 1981 to 2016.

Atmospheric gravity waves (GWs) are linear, internal waves in the stably stratified atmosphere (Hines, 1960). They are established and maintained by the gravitational and buoyancy forces. Tropospheric disturbances such as thunderstorms or air flow over mountains (e.g., Fritts & Alexander, 2003) are common sources and occur worldwide. In addition, TCs and their associated convection are well-known sources of GWs (Dewan et al., 1998; Espy & Huppi, 1997; Taylor & Hapgood, 1988).

GWs are an important coupling mechanism for the transfer of energy and momentum from the lower to the upper atmosphere. The propagation and dissipation of GWs couple the troposphere with the Earth's middle and upper atmosphere (including the stratosphere, mesosphere, thermosphere, and ionosphere) dynamically and electrodynamically (Vadas & Liu, 2009; Vadas & Nicolls, 2009). Some GWs having relatively small amplitudes can propagate into the stratosphere, mesosphere, and thermosphere and deposit their momentum and energy via wave breaking or viscous damping into the mean flow. Such processes drive the atmosphere out of radiative balance and create significant temperature and wind changes

(Holton, 1982; Lindzen, 1981; Vadas & Liu, 2009). In this way, GWs play a key role in determining the atmospheric circulation, wind and temperature structure, and turbulence and chemistry of the stratosphere, mesosphere, and thermosphere (e.g., Alexander et al., 2010; Fritts & Alexander, 2003; Vadas et al., 2014). GWs can also induce disturbances in the plasma velocities and densities in the ionosphere, creating traveling ionospheric disturbances (TIDs, e.g., Hines, 1960; Djuth et al., 1997; Nishioka et al., 2013; Nicolls et al., 2014), thereby impacting communication as well as Global Navigation Satellite Systems (Jin et al., 2015).

The scientific literature is replete with studies of TC-generated GWs, extending from the upper troposphere and stratosphere into the mesosphere. Aircraft, radiosonde, and radar observations have detected wind and temperature disturbances in the upper troposphere and lower stratosphere associated with TCs (Chane-Ming et al., 2002; Chun et al., 2007; Dhaka et al., 2003; Pfister et al., 1993; Sato, 1993). Besides temporal and spatial correlation studies near TCs, modern nadir sounding techniques provide a direct way to trace GWs back to specific sources of convection within a TC. The Atmospheric Infrared Sounder (AIRS) on National Aeronautics and Space Administration's (NASA) Aqua satellite observed concentric GWs in the stratosphere emanating from TCs in $CO_2$ absorption bands. (Hoffmann et al., 2018; Kim et al., 2009; Wu et al., 2015; Yue et al., 2014). Satellite observations of stratospheric TC GWs compare directly to mesoscale numerical models (e.g., Advanced Research Weather Research and Forecasting and Mesoscale Model; e.g., Kuester et al., 2008; Kim et al., 2009; Kim & Chun, 2010). The horizontal wavelengths of TC-generated GWs can range from order 10 to $10^3$ km. The frequency of a GW from a cyclone can range from high to inertial, with a period ranging from a few minutes to longer than 1 day. However, these mesoscale numerical models often have an upper cap below the mesopause. The airglow layers enable the observations of TC GWs in the mesopause from both the ground and space.

Ground-based airglow imagers in Japan observed typhoon excited GWs at the mesopause (Suzuki et al., 2013). From the top-down perspective, two visible and near infrared (NIR) band sensors in space—(1) the Day/Night Band (DNB, Miller et al., 2013) of the Visible Infrared Imager Radiometer Suite (VIIRS) on board the Suomi National Polar-orbiting Partnership (Suomi NPP) satellite and (2) the Visible-light and Infrared Spectrum Imager of International Space Station Ionosphere, Mesosphere, Upper Atmosphere and Plasmasphere Mapping Mission—have observed a large number of TC GWs at the mesopause globally (Lai et al., 2017; Miller et al., 2015; Perwitasari et al., 2015; Yue et al., 2014). Both mesoscale (40- to 60-km horizontal wavelength) and synoptic scale (~500-km wavelength) GWs were observed over TC Mahasen (2013) in the Bay of Bengal (Yue et al., 2014). Due to the height limitation of current mesoscale models, which often employ an upper cap below the mesopause, no direct comparisons between GW-resolving models and observed TC GWs at the mesopause have been attempted.

GW-induced ionospheric perturbations over TCs have also been long recognized. Bauer (1958) find an increase of foF2 (critical frequency of the ionospheric $F_2$ layer) during a passage of a hurricane. Hung and Kuo (1978) observed TIDs in the $F$ region ($F_2$ layer peak height is generally at the altitude of ~300–500 km) and traced the source of the underlying GWs back to a hurricane. Bishop et al. (2006) carry out a comprehensive study of ionospheric perturbations from a tropical storm using an incoherent scattering radar at the Arecibo Observatory. Strong variations in the $F$ region plasma densities, electric field and plasma drift, and spread of $F$ region scintillations were observed during the storm's passage over Puerto Rico. Vadas and Crowley (2010) investigate traveling ionospheric disturbances (TIDs) observed in the $F$ region over Wallops Island, concluding that the underlying GWs were secondary GWs from Tropical Storm Noel. Nishioka et al. (2013) discover circular waves in the total electron content (TEC) over Moore, Oklahoma, lasting for more than 7 hr and conclude that the underlying GWs were created by deep convection of a tornadic thunderstorm. Recently, the ground-based Global Navigation Satellite Systems network in certain areas (e.g., Japan, continental United States, Taiwan, mainland China, and western Europe) has observed TIDs near TCs [Chou, Lin, Yue, Chang, et al., 2017; Song et al., 2017]. The concentric structure of these TIDs helps to confidently attribute their source to nearby TCs, and thus a powerful tool in GW coupling studies. However, these are mostly cause and effect studies without knowledge of the characteristics of the TC-induced GWs in the stratosphere, mesosphere, and thermosphere. Therefore, the specific physical mechanisms for the TC GW excitation and ensuing propagation related to the observed GW perturbations middle to upper atmosphere remains unclear.

Given the increasing number of satellite instruments that can observe GWs, the detection of GWs at various heights in the middle and upper atmosphere has become increasingly feasible and accurate. In this paper, we describe the GWs launched from Hurricane Matthew as observed in the stratosphere, mesosphere, and ionosphere using various ground-based and satellite observations. The characteristics of the hurricane-induced GWs at different heights and times by way of various observations are diagnosed in detail toward gaining a better understanding of the aforementioned physical mechanisms and linkages between the observables and the underlying processes.

In this paper, we report on the Hurricane Matthew-induced GWs event that occurred during October 2016. In section 2, we introduce the data sets from satellites and ground-based Global Positioning System (GPS) receivers that we used in this study. Section 3 briefly describes some background knowledge about Hurricane Matthew. Section 4 presents observations from satellites and ground-based GPS-TEC measurements taken during the Hurricane Matthew event. Discussions concerning the observed GW and TEC TIDs are presented in section 5. Conclusions of the findings are presented in section 6.

## 2. Satellites and GPS Data Sets

### 2.1. Aqua/AIRS

The NASA Aqua satellite, the first of six satellites currently flying as the *A-Train* constellation, was launched from the Vandenberg Air Force Base in California in 2002. Aqua flies in a 705-km-altitude Sun-synchronous polar orbit with 98.8-min orbital period and an inclination of 98.2°. Its local time ascending node (LTAN; equatorial crossing) is ~01:30 p.m., thus providing a ~01:30 a.m. descending node. With its ~99-min orbital period, Aqua achieves nearly global coverage via 14.5 orbits per day (Aumann et al., 2003).

The AIRS carried on board Aqua is a cross-track scanner of infrared sounder. Each scan or *swath* is 1,780 km (±49.5° wide, according to Hoffmann et al., 2014). Its swath data consist of 90 footprints that are measured over a 2.667-s duration per scan. The along-track distance between adjacent scans is 18 km. The horizontal resolution of the AIRS footprints is 13.5 × 13.5 km at nadir and 41 × 21.4 km at the scan edges, respectively. AIRS data are packaged as *granules* composed of 135 scans and thus 2,400 km of along-track data. These granules are concatenated to produce longer tracks of information for the current analysis.

Each footprint AIRS measures an infrared spectrum of the thermal emissions integrated from the Earth surface to the atmosphere. To fulfill its atmospheric sounding requirements, AIRS provides 2,378 channels covering the wavelength ranges of 3.74–4.61, 6.20–8.22, and 8.8–15.4 μm at high spectral resolution of $\lambda/\Delta\lambda = 1{,}200$ (Aumann et al., 2003). These hyperspectral measurements enable accurate characterization of temperature and trace gas profiles compared to previous satellite sounding instruments.

### 2.2. Suomi NPP/VIIRS DNB Low-Light Visible

The Suomi NPP satellite, developed by NASA and is operated by the National Oceanic and Atmospheric Administration (NOAA), is the first satellite in NOAA's latest generation Joint Polar Satellite System operational program. Suomi NPP flies at an altitude of 834 km in a Sun-synchronous polar orbit with a 98.7° inclination. It orbits the Earth every 101.44 min and completes 14.2 orbits per day (Trishchenko & Garand, 2012). Like Aqua, Suomi NPP has an LTAN of ~01:30 p.m. ascending node and corresponding ~01:30 a.m. descending node. Suomi NPP carries the Visible Infrared Imaging Radiometer Suite (VIIRS), a 22-band imaging radiometer that measures radiation, the infrared and visible light (Lee et al., 2006; Miller et al., 2013). The DNB sensor detects extremely faint light within its 505–890-nm band pass. Each of its 16 detectors has a spatial resolution of 742 × 742 m. The synchronous scanning by the 16 detectors produces ~12-km-long and 3,040-km-wide along-track swaths that are oriented perpendicular to the flight direction (i.e., cross track, Seaman & Miller, 2013).

It is an unforeseen windfall that the detector's sensitivity to the nightglow emissions at altitude of 85–90 km on moon-free nights, which ranges from $10^{-5}$ to $10^{-7}$ $W{\cdot}m^{-2}{\cdot}sr^{-1}$, is extremely high. Also, its horizontal spatial resolution is uniform across the entire swath from nadir to both edges. This allows us to explore the subkilometer-level details of GWs with vertical wavelengths longer than ~10 km (Miller et al., 2015), when the GWs modulate the airglow layer in the mesopause region.

### 2.3. GPS TEC

While small-scale GWs are likely to dissipate or break below the stratopause, medium and/or large-scale GWs having large horizontal phase speeds and vertical wavelengths can propagate upward from their sources into the thermosphere under favorable wind conditions (Azeem et al., 2015; Fritts & Vadas, 2008; Nishioka et al., 2013; Vadas, 2007). Although these *primary* GWs can have concentric ring structure while in the stratosphere and mesosphere, these ring structures may be substantially altered into partial rings by the time these GWs propagate in the thermosphere (Vadas & Liu, 2009). Additionally, some of these GWs dissipate from molecular viscosity in the lower thermosphere, thereby exciting secondary GWs having larger horizontal scales and phase speeds (Vadas & Liu, 2009, 2013).

When primary or secondary GWs propagate in the thermosphere, they pull and push the ions in the ionosphere along the Earth's magnetic field lines, thereby creating oscillations in the ions and electrons called TIDs (Crowley & Rodrigues, 2012; Hocke & Schlegel, 1996; Nicolls et al., 2014; Vadas & Nicolls, 2009). Such TIDs are not self-sustaining but rely on the underlying GW to maintain them.

For the Hurricane Matthew event we investigate here, we also utilize GPS-TEC data from over 4,000 GPS sites in the contiguous United States (CONUS) to identify and analyze the TIDs above the receivers. Slantwise TEC information is derived from the pseudorange and phase measurements of GPS signals at L1 (1575.42MHz) and L2 (1227.6 MHz) frequencies. Then, the slantwise TEC is converted to the vertical TEC by using the obliquity factor model from Kaplan and Hegarty (2005). The International Reference Ionosphere (IRI) model (Bilitza et al., 2011) is used to project the slantwise TEC to vertical TEC via assuming that the height of the maximum of the $F_2$ layer (hmF2) in the IRI model is the altitude of the ionospheric pierce point. We detrended the perturbations in the TEC by applying 40-min running mean averages for each GPS satellite. We then applied a nearest-neighbor interpolation onto a 0.15° × 0.15° latitude and longitude grid and smoothed the gridded data using a 2-D Gaussian filter with a full-width at half maximum of 3° (Azeem et al., 2017; Nishioka et al., 2013). Finally, we applied an adaptive complex diffusion despeckling filter (Azeem & Barlage, 2018).

## 3. Hurricane Matthew Overview

Before becoming the first Saffir-Simpson scale Category 5 Atlantic hurricane since Hurricane Felix in 2007, Matthew initially started as a tropical wave off the coast of Africa on 23 September 2016. According to the record of Stewart (2017), it formed in the Caribbean Sea on 28 September and then reached its peak wind speed at ~74.6 m/s at 00:00 UTC on 1 October. Matthew made landfalls along the coasts of Haiti, Cuba, and western Grand Bahama Island, and finally degraded to a Category 1 hurricane just offshore South Carolina. Near its end, Matthew weakened gradually and transitioned into an extratropical cyclone system. Matthew brought heavy rainfall and devastation along its path through the Caribbean, with Haiti and specifically its Tiburon Peninsula receiving more than 20 inches (50.8 cm) of rain (Stewart, 2017).

Figure 1 shows the track of Hurricane Matthew with four analysis points per day. Triangles and asterisks show the positions of its eyewall at 12:00 UTC and 00:00 UTC each day, respectively. The radii of the circles denote the maximum sustained surface wind speed from multimeasurements records (see more in Stewart, 2017; Figure 2) of Matthew at each location. The three stages of the hurricane's life span (tropical storm, hurricane and extratropical cyclone/low-pressure system) are shown by green, purple, and red portions of the trajectory, respectively. Hurricane Matthew's positions are taken from Stewart (2017).

Figure 2 shows the maximum sustained surface wind speed, hurricane eyewall pressure, eyewall movement speed, and radius of maximum wind throughout the hurricane life span. The first three parameters are taken from Stewart (2017) and the latter parameter (radius of maximum wind) is from the *Extended Best-Track data set* developed by Demuth et al. (2006). After Hurricane Matthew reached Stage 2 (hurricane) on 29 September, it took only ~1 day to further intensify into a Category 5 storm. During this period of rapid intensification, shown in Figure 2 as red shading, we hypothesize that the strong latent heating associated with the deep convection in the hurricane excited many GWs. In this study, we will investigate if the GW activity was more intense when Hurricane Matthew intensified.

Among the published studies of Hurricane Matthew, Miller et al. (2018) conducted a preliminary analysis of the DNB's unique remote sensing capability. Owing to the high sensitivity and high spatial resolution of the low-light

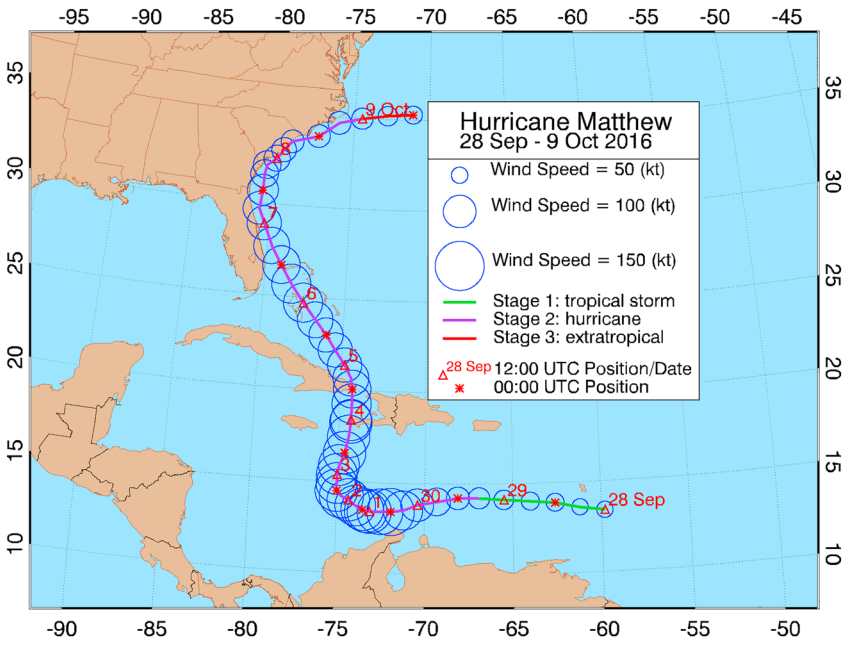


**Figure 1.** Trajectory and wind velocity (unit: knot, 1 kt = 1.852 km/hr) of Hurricane Matthew from 28 September to 9 October 2016, based on multimeasurements data retrieved from Stewart (2017).

visible DNB observations, they noted fine structures in the visible-light-band airglow layer due to hurricane-induced GWs. They also demonstrated the DNB's ability to identify the widespread power outages caused by the hurricane winds and flooding. Their analysis includes a photograph from Puerto Rico by which GWs in the airglow and lightning-induced sprites were observed simultaneously, correlated with a semipersistent convective feature on the east flank of Hurricane Matthew. In addition of this, Huang et al. (2018) also contributed their new discoveries of the ground-based observation of sprites over Hurricane Matthew.

## 4. Satellite Observations

### 4.1. AIRS Observations

According to Dewan et al. (1998), the 4.3-μm $CO_2$ absorption band is particularly well suited to detecting GW disturbances in the stratosphere. The AIRS channels selected in this study, sampling this $CO_2$ band, are most sensitive to temperatures at 30–40 km of altitude (Hoffmann & Alexander, 2009, 2010)—in the middle stratosphere. GW signals were revealed in the AIRS data by subtracting a fourth-order polynomial fit to the 4.3-μm brightness temperatures (BTs) along each across-track scan. Doing so removes slowly varying signals, for example, caused by planetary waves or large-scale temperature gradients (Hoffmann et al., 2013; Hoffmann & Alexander, 2010). Due to the relative coarse spatial resolution, AIRS can only detect

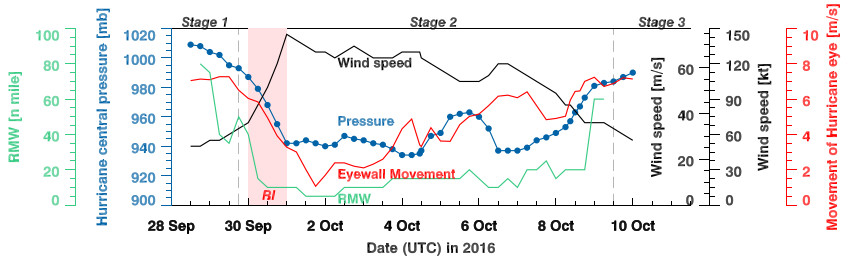


**Figure 2.** Maximum sustained surface wind speed (black), hurricane eyewall pressure (blue), eyewall movement speed (red), and radius of maximum wind (green) of Hurricane Matthew life span. The three stages of Hurricane Matthew are divided by vertical dashed lines. Each data type corresponds to a *Y* axis in the same color. The period of rapid intensification (RI) is shown via red shading.

GWs with vertical wavelength longer than ~20 km and horizontal wavelengths ~50–1000 km (Yue et al., 2013). Figure 3 shows the AIRS 4.3-μm BT perturbation (left column) and corresponding cloud brightness temperature observations in the 8.1-μm atmosphere window band (right column) for Hurricane Matthew as sampled over the period 1–2 October 2016. The green crosses denote the position of hurricane eye at 6 or 18 UTC when the satellite was approximately passing over the hurricane.

In Figures 3a and 3b, the narrow swath width of each AIRS scan (~1,780 km) results in a coverage gap between adjacent orbits. Here the swath east of 70°W was observed ~100 min prior (~05:37 UTC) to the swath to the west of the gap (~07:15 UTC). Ring-like features are easily discernable in the 4.3-μm BT perturbations west of the gap, indicating convectively induced CGWs. Despite the time difference between the swaths, the ring-like features also appear connected across the two swaths, although they are quite weak on the swath east of the gap and are only apparent at ~64°–66°W and ~13°–18°N. Four red circles are drawn upon Figure 3a to identify the wavefronts having radii of 460, 660, 860, and 1,060 km from the hurricane center (identified as a green cross) at 6:00 UTC on 1 October. These four wavefronts are centered on the deep convection within the hurricane and are therefore most likely associated with the hurricane-induced GWs that are propagating through the stratosphere. The fact that the rings are quite weak east of the gap may occur for several reasons. The first is that the largest-amplitude CGWs are the inner rings, but the inner rings of the eastward propagating CGWs cannot be seen because they would have been located directly in the gap. The second is that a background wind with a significant zonal component would have affected the eastward propagating CGWs differently than the westward propagating CGWs. For example, if the background wind is eastward, then it would cause $\lambda_z$ of the eastward propagating GWs to decrease. If this wind is strong enough, then (a) $\lambda_z$ could decrease enough to be below AIRS's observing threshold or (b) the GWs could be eliminated due to critical level filtering (e.g., Fritts & Alexander, 2003). Note that there are also northwestward propagating CGWs in the northern portion of the swath east of the gap at 55–65°W and 15–30°N; these GWs are likely excited by convective plumes not associated with the hurricane, because they have an apparent center at ~(55°W, 20°N), which is ~2,000 km from the hurricane center at that time.

In Figure 3a, only the inner two of four rings of the CGWs structure are strongly visible, while the outer two rings are rather weak. To characterize the wave structure more rigorously, a 2-D fast Fourier transformation (FFT) analysis is applied to the AIRS perturbation data within the yellow rectangular area shown in Figure 4a. This region is enlarged in Figure 4b, where the $x$ and $y$ directions represent the cross-track (at an azimuth of ~105°) and along-track (at an azimuth of ~15°) directions, respectively. The normalized FFT power of Figure 4b is shown in Figure 4c. The power peak highlighted within the yellow circle shows that the largest-amplitude GWs propagated mainly in the cross-track direction, with a dominant horizontal wavelength of ~204 km ($\lambda_H = 2\pi/\sqrt{{k_x}^2 + {k_y}^2}$, in which $k_x = 3 \times 10^{-2}$ and $k_y = 0.7 \times 10^{-2}$ km$^{-1}$). The peaks near the yellow circle are also GWs with horizontal wavelengths of ~200–220 km (e.g., $k_x = 2.25 \times 10^{-2}$ and $k_y = -1.8 \times 10^{-2}$ km$^{-1}$) but with larger uncertainties. In order to make sure that the dominant wavelength ~200 km is accurate, we also made an improvement in the 2D FFT analysis. A projection was applied to the AIRS perturbation data within the red circular trapezoid area shown in Figure 4a before another 2D FFT analysis. The circular trapezoid region is enclosed by azimuth 230–340° and distance of 448–1,500 km from the hurricane eye. Then as shown in Figure 4d, it was projected onto a rectangular coordinate system with respect to axes of distance from the hurricane eye ($x$ direction in coordinate) and azimuth relative to the hurricane eye ($y$ direction in coordinate) by a quadrangle bilinear interpolation (5-km intervals in the radius direction and 0.5° intervals in the azimuth range). The normalized 2-D FFT power of Figure 4d is shown in Figure 4e, in which two clear centrosymmetric hot spots at $k_x \approx 3 \times 10^{-2}$ and $k_x \approx -3 \times 10^{-2}$ km$^{-1}$, which means $\lambda_x = 2\pi/k_x \approx 210$ km. According to the full-width at half maximum of the peak in spectrum, the dominant wave represented by the peak has an uncertainty of ~±20 km. Besides, the hot spots reside at $k_y = 0$ degree$^{-1}$ are consistent with the parallel wave pattern in Figure 4b, which means that the wavefronts in Figure 4a are propagating in all directions from the center of the hurricane eye.

Although CGWs were seen at 07:15 UTC on 1 October, they were not seen in most other AIRS scans during the hurricane's lifetime. This could be for several reasons. It could have been caused by the limited observation field due to AIRS' relatively low orbit or to its coarse resolution and the presence of GWs with smaller horizontal scales. For example, the images at 18:06 UTC on 1 October show arc-like GWs that do not span a large azimuthal angle (and therefore cannot be called concentric rings, see Figures 3c and 3d). Additionally,

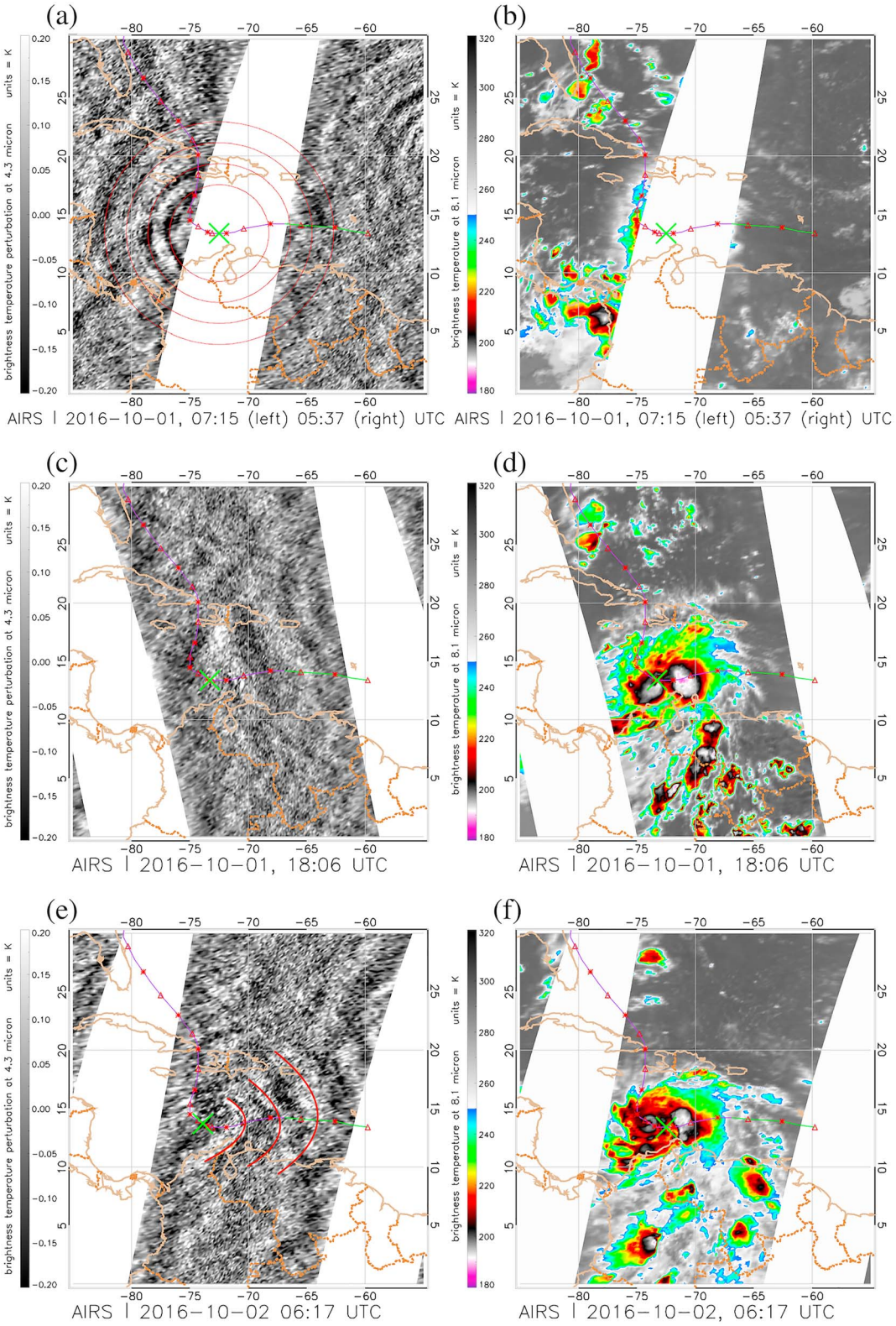


**Figure 3.** AIRS brightness temperature perturbation at 4.3-μm band (left column) and cloud top temperature at 8.1 μm (right column, unit: K). Rows 1–3 correspond to 07:15 UTC 1 October (Figures 3a and 3b), 18:06 UTC 1 October (Figures 3c and 3d), and 06:21 UTC 2 October (Figures 3e and 3f) 2016, respectively. The colored curve in each map is the trajectory of Hurricane Matthew. Four red circles in the first map are distance contours of 460, 660, 860, 1,060 km from the hurricane eye. Here the hurricane center is shown with a green cross. AIRS = Atmospheric Infrared Sounder.

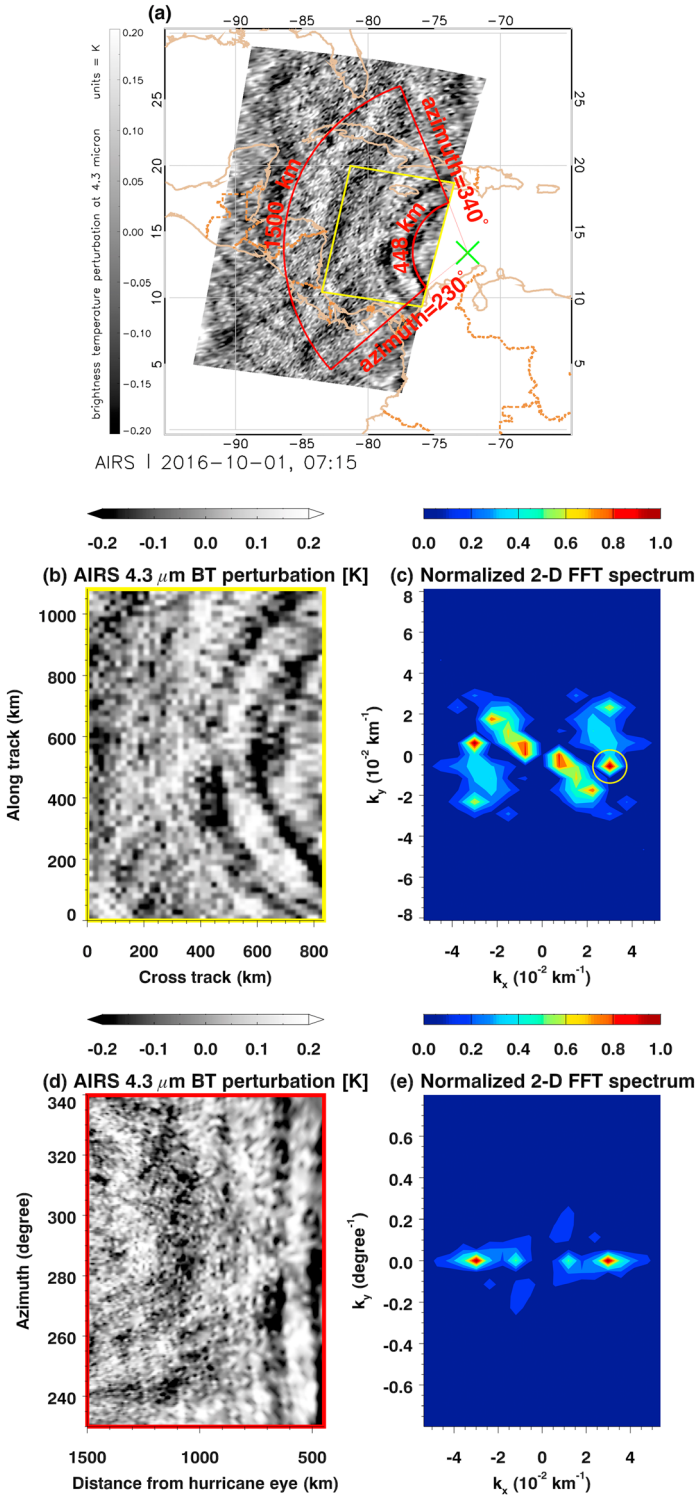


**Figure 4.** (a). AIRS 4.3-μm BT perturbation data observed at 07:15 UTC on 1 October, the same as Figure 3a. (b). Equal interval resampling of AIRS 4.3 micron BT perturbation data of yellow rectangular area in Figure 4a, where *x* direction is at an azimuth of ~105° (cross track) and *y* direction is at an azimuth of ~15° (along track). (c). The 2-D FFT spectrum of Figure 4b. Hot spot in yellow circle denotes the highest spectrum peak at wavelength ~203 km. (d). Perturbation data projected onto a rectangular coordinate with respect to axes of the distance from the hurricane eye (*x* direction in coordinate) and azimuth relative to the hurricane eye (*y* direction in coordinate). The data are from the red circular trapezoid area in Figure 4a. (e). The 2D FFT spectrum of Figure 4d. AIRS = Atmospheric Infrared Sounder; FFT = Fourier transformation; BT = brightness temperature.

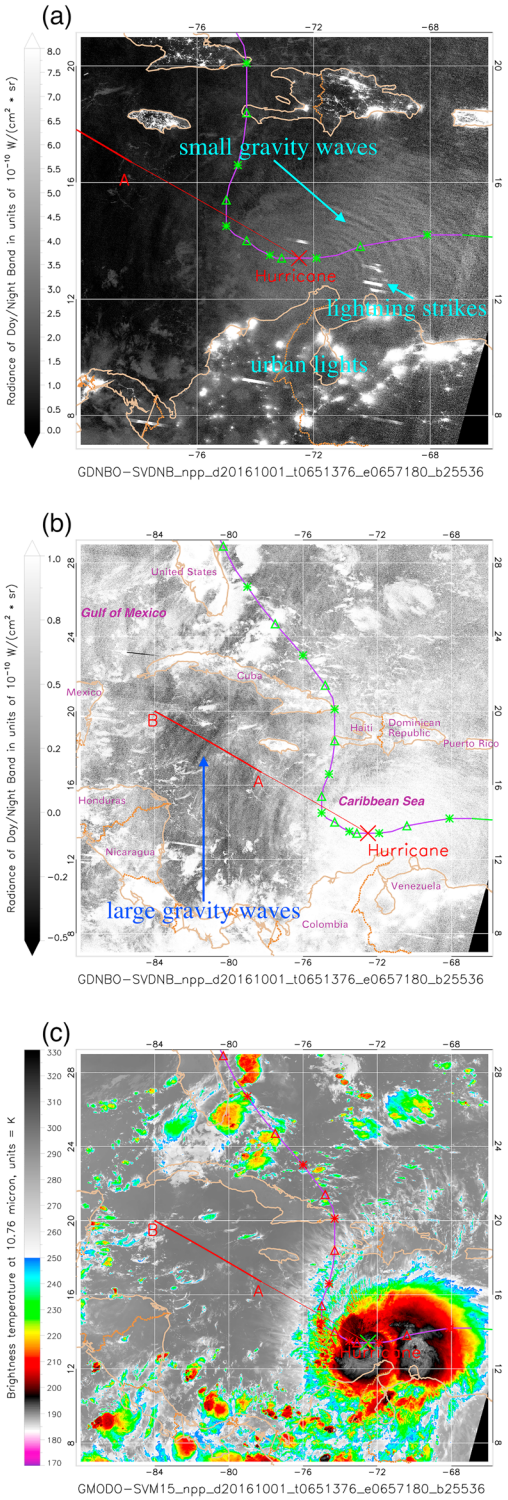


**Figure 5.** (a). Concentric gravity waves detected by VIIRS/DNB at 06:51 UTC on 1 October 2016. The red solid line *Eye-A-B* is a section of a Great Circle oriented from hurricane eye (13.4°N, 72.5°W) to point B (20°N, 84°W). Thin red line: from hurricane eye to point A, thick red line: from A to B. (b). The same as Figure 5a but in a larger colorbar range and larger map scale focused on hurricane region. (c). Simultaneous cloud brightness temperature at NPP M15 band (10.76 μm). The colored line in Figures 5a–5c shows the trajectory of hurricane.

the images at 06:21 UTC on 2 October show some weak or distorted concentric structures emanating eastward from the hurricane eye (see Figures 3e and 3f). These are likely *arc-like* and *squashed* ring patterns that were originally concentric ring GWs but were altered by strong intervening winds (Vadas et al., 2009).

### 4.2. VIIRS DNB Observations

GW propagation through or along the mesopause can produce fluctuations in the airglow brightness (Miller et al., 2015). Figures 5a and 5b show a VIIRS/DNB imagery collected at 06:51 UTC on 1 October. Fine luminous concentric structures are noted to the east of Hurricane Matthew's eye (red cross). In Figure 5a, we also see the dense urban lights on the South American shore, and the white segments are caused by DNB sensor scans through active lightning strikes that illuminate the tops of the regional clouds. These data were collected at New Moon phase, when no moonlight in the scene. The clouds around Matthew's eye were illuminated instead by the backscattering of light from the downwelling airglow and also starlight (e.g., Miller et al., 2012).

Due to the extremely high resolution provided by the DNB, very small wave structures were also observed. Miller et al. (2018) analyze the GW ripple wave pattern seen in Figure 5a (*small GWs* notation) on the eastern side of Matthew's eye and north of Venezuela, determining a wavelength of 24–27 and 30 km. These ripple-pattern structures are distributed to the northeast of the hurricane eye. As the greyscale colorbar of Figure 5a shows, the brightness is 0–8 $\times$ $10^{-10}$ W·cm$^{-2}$·sr$^{-1}$, similar to variation observed for the multisource GW-modulated DNB nightglow imagery considered by Miller et al. (2015).

Fluctuations with larger wavelength are also seen in Figure 5b, far to the northwest of Matthew and above the open ocean south of Cuba. However, the brightness is so faint that negative data values occur due to slight DNB calibration errors at these very low (near the noise floor) radiance values. Only a colorbar with allowance for small negative values ($-0.5 \times 10^{-10}$ to $1.0 \times 10^{-10}$ W·cm$^{-2}$·sr$^{-1}$) can show this northwestward wave structure. By varying the DNB map scale, we can see both small- and large-scale waves (with horizontal wavelengths of 30–200 km) simultaneously, a result that is consistent with DNB observations of cyclone Mahasen (Yue et al., 2014).

Figure 5c shows the corresponding thermal infrared BTs from the VIIRS M15 band (10.76 μm). It shows the cloud top BTs for Hurricane Matthew at the same time as in Figure 5a. In this image, red and black regions denote deep convection. The lower the temperature, the higher the top of the cloud.

To characterize the large-scale northwestward wave perturbations in the airglow layer, we calculated perturbations at 0.5-km intervals from the hurricane eye to the point B (20°N, 84°W; marked along the red line in Figure 5b) and extracted the DNB brightness value every 0.5 km by using a quadrangle bilinear interpolation on the DNB data grid. There are altogether 2,800 points (covering 1,400 km) from the eyewall to point B.

Figure 6 shows results of DNB data along the transect shown in Figure 5. The green curve in Figure 6a shows the Earth surface brightness temperature, including cloud top surface and ocean surface at the boundary of ~700 km from the hurricane eye. For convenience of analysis, the first

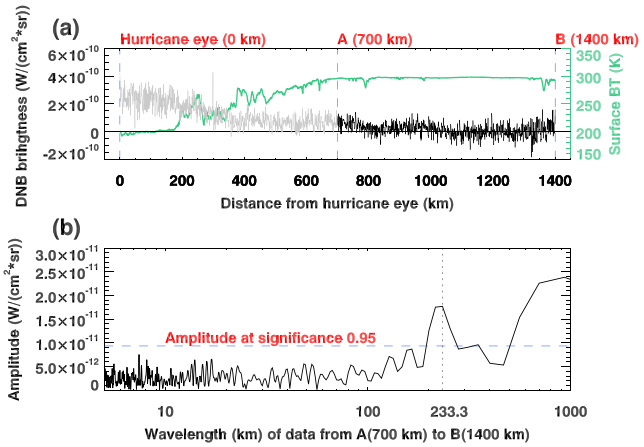


**Figure 6.** (a). NPP M15 band brightness temperature (green) and VIIRS/DNB brightness (gray and black) from hurricane eye (13.4°N, 72.5°W) along the great circle line to point B (20°N, 84°W) from Figure 5a (unit: $W{\cdot}cm^{-2}{\cdot}sr^{-1}$) with spatial step length 0.5 km using quadrangle interpolation in DNB data grid. (b). Lomb-Scargle periodogram of the DNB brightness along A–B from Figure 6a.NPP = National Polar-orbiting Partnership; DNB = Day/Night Band; VIIRS = Visible Infrared Imager Radiometer Suite.

half of the points (Hurricane-A part, 700-km-long, light gray portion of radiance data shown in Figure 6a) from hurricane eye are cut off, as they are contaminated by the hurricane cloud top reflectance. Figure 6b shows a Lomb-Scargle periodogram analysis applied to the brightness for the remaining data points (see Lomb, 1976; Scargle, 1982). The analysis shows a peak at ~233 km horizontal wavelength. As no periodic cloud structures exist along the A-B transect in Figure 5c, we can assert that the wave patterns derived by the Lomb-Scargle periodogram are associated with the GW structures seen in Figure 5b.

As first mentioned by Miller et al. (2018), similar 30–200 km CGW patterns were detected in the vicinity of Hurricane Matthew on almost every night during 2–7 October period in the DNB images. These data are shown in Figure 7. However, unlike Miller's study that takes a broader perspective on the DNB's novel nighttime remote sensing capabilities, here we focus on specific utility of DNB imagery to characterize the GWs properties of Hurricane Matthew.

### 4.3. GPS-TEC Concentric TIDs (or CTIDs)

Figure 8 shows the wavefronts of CTIDs over the CONUS, as observed by surface-based GPS TEC measurements at 06:00 UTC on 1, 2, and 7 October 2016. The red circles have radii of 3,000 and 3,200 km from Matthew's eye as analyzed at 06:00 UTC on 1 and 2 October, respectively, and of 1,200 and 1,400 km at 06:00 UTC on 7 October 2016. The color scale on these panels is ±0.01 TECU (1 TECU = $1 \times 10^{16}$ el $m^{-2}$). The figures represent the weighted (and smoothed) sum of the TEC fluctuations over the map grid, while the unsmoothed amplitude of the TIDs is about ±0.05 to 0.07 TECU. As the hurricane approached the southeast coast of the United States, the distance from the hurricane source to the CTIDs wavefronts also decreased. The consistency of the CTIDs patterns implies that they were excited from a single source or an interacting cluster of deep convective plumes in close proximity. Note that the estimated centers of the CTIDs agree well with the position of the hurricane eye for all 3 times, which allows us to infer Hurricane Matthew as their source as long as wind effects are unimportant.

To better understand the time dependence of the wave distribution, we analyze the GPS-TEC data in the meridional (80°W, 33–41°N) and in the zonal (90–75°W, 37°N) directions, shown as red lines in Figure 9a. Additionally, the positions of Hurricane Matthew at 6:00 UTC on 1, 2, and 7 October are shown as black crosses in Figure 9a. The time-latitude and time-longitude slices of the GPS-TEC data (called "keograms") on these 3 days are shown in Figures 9b and 9c, 9d and 9e, and 9f and 9g, respectively.

In Figure 9, well-defined and long-lasting wave structures are observed at ~5–8 UTC on 1 October, ~4–8 UTC on 2 October and ~0–9 UTC on 7 October. These TIDs on three different days correspond closely to the GWs observed on 2–7 October by VIIRS DNB in Figure 7. Using an FFT analyses, we calculated the periods $\tau$ and the zonal ($c_x$) and meridional ($c_y$) phase speeds of the TIDs on 1, 2, 7 October 2016 from Figure 9. Here we compute the horizontal phase speed from the keograms using equation 13 from Vadas and Becker (2018): $c_h = 1/\sqrt{1/c_x^2 + 1/c_y^2}$. We then compute the horizontal wavelengths via $\lambda_h = c_h\tau$. We found that the TID ground-based periods, phase speeds, and horizontal wavelengths were as follows: (i) ~30 ± 4 min, ~189 ± 17 m/s, and ~340 ± 30 km on 1 October, (ii) ~24 ± 4 min, ~192 ± 37 m/s, and ~270 ± 50 km on 2 October, and (iii) ~27 ± 4 min, ~157 ± 26 m/s, and ~250 ± 40 km on 7 October, respectively. These results indicate that the horizontal phase speed for the GWs was between 100 and 200 m/s, that the horizontal wavelength was between 250 and 350 km, and that their period was between 15 and 60 min. Note that the most of the parameters for these different TID events are similar within the experimental errors. This is similar to the results from model studies (Vadas & Liu, 2013) and observations (Vadas & Crowley, 2010) of GWs from deep convection and a tropical storm, respectively. Given these characteristics, we classify these TIDs as medium scale (Hocke & Schlegel, 1996).

In Figure 10, the Horizontal Wind Model 2014 (HWM14, Drob et al., 2015) shows the horizontal wind components at the Mathew's eye and at a fixed position (80°W, 37°N) at 06:00 UTC on 1, 2, and 7 October 2016.

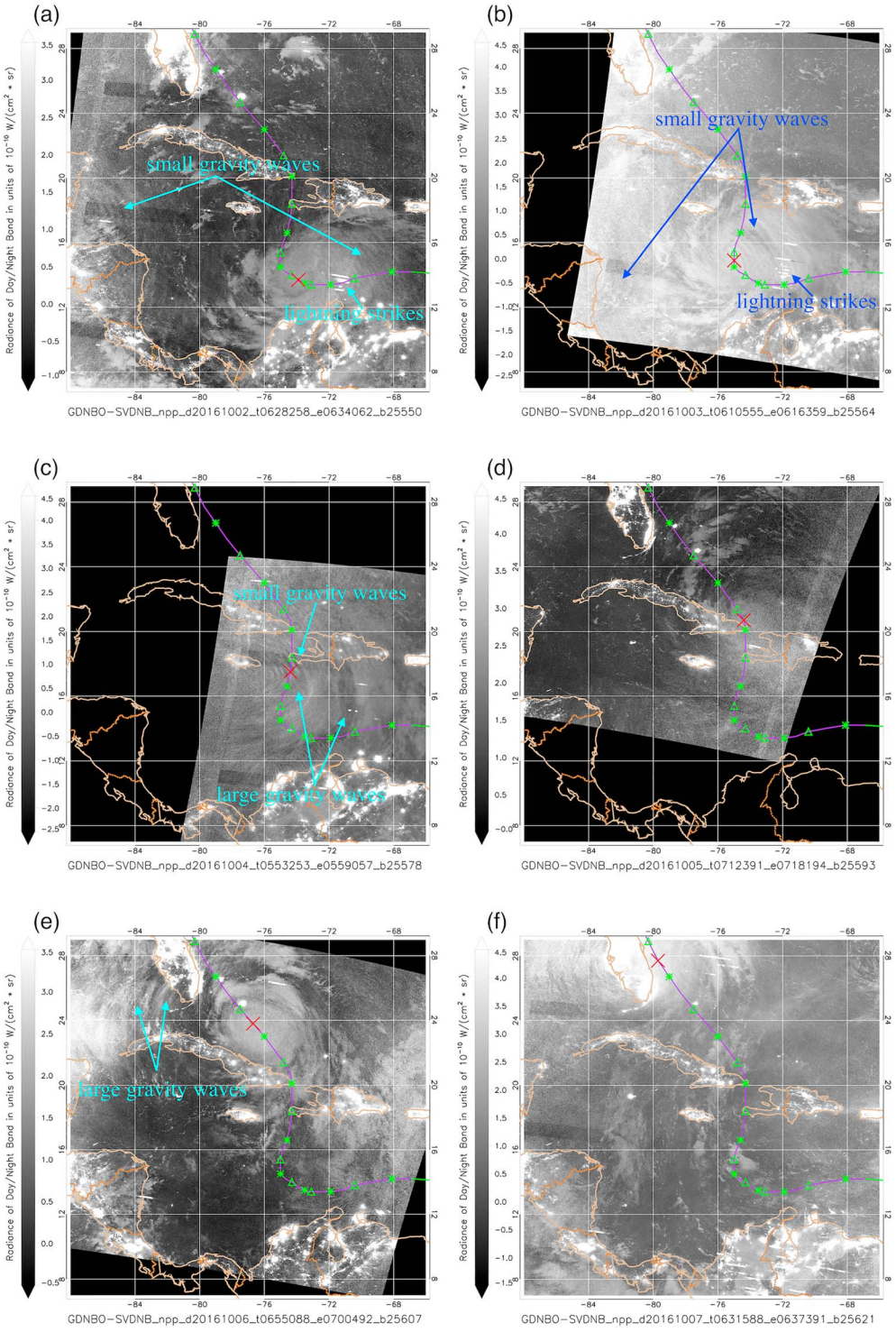


**Figure 7.** Different scales GWs detected by VIIRS/DNB channel in the region of Caribbean Sea. Six figures correspond to 2–7 October 2016, respectively. DNB = Day/Night Band; VIIRS = Visible Infrared Imager Radiometer Suite; GWs = gravity waves.

We infer that on both 1 and 2 October, even the maximum of wind velocity over Hurricane Matthew eyewall region at $z = 0$–$500$ km is considerably smaller than the horizontal phase speed of the GWs. Therefore, the GWs were able to propagate deep into the thermosphere without being critical level filtered by the prevailing winds; therefore, dissipative filtering from rapidly increasing kinematic viscosity in the thermosphere will

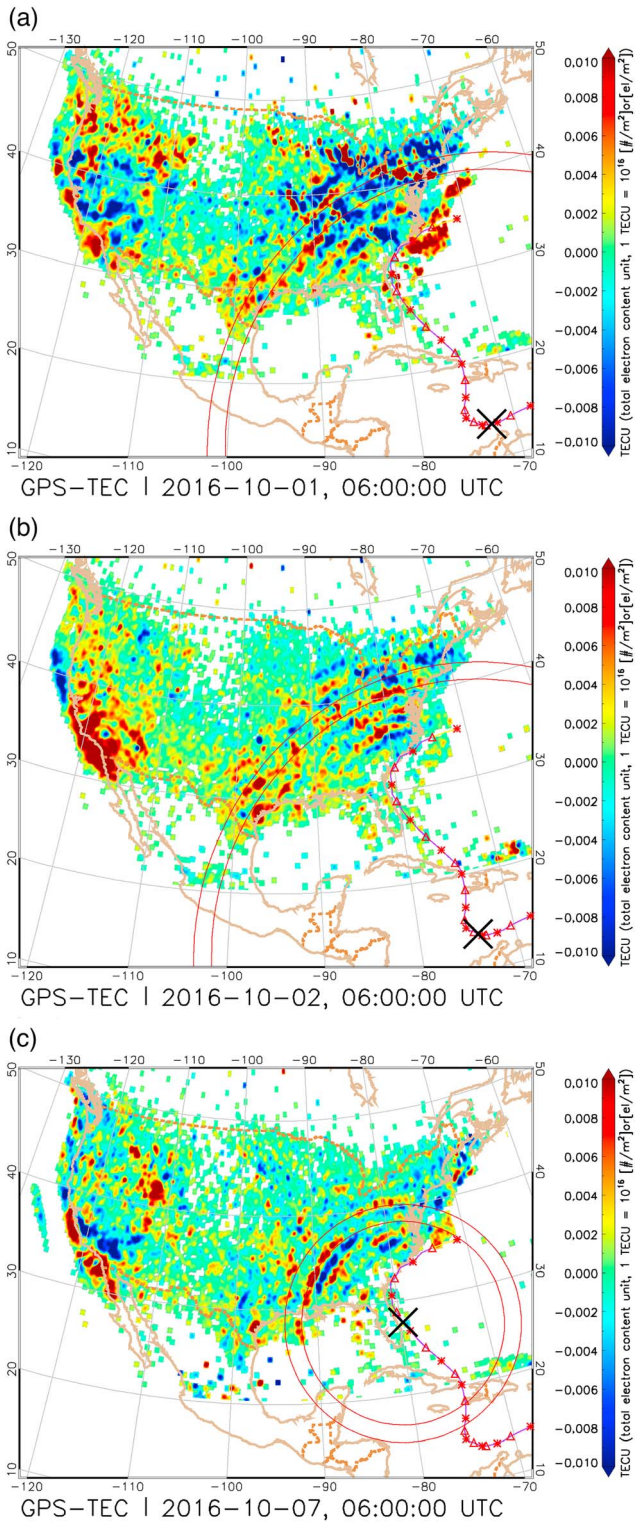


**Figure 8.** GPS TEC perturbation showing concentric wavefronts over CONUS at 06:00 UTC on (a) 1 October 2016, (b) 2 October 2016, and (c) 7 October 2016, respectively. Black cross denotes the position of hurricane eye at each time. As a reference, the red circles have radii of (a) 3,000 and 3,200 km, (b) 3,000 and 3,200 km, and (c) 1,200 and 1,400 km from hurricane eye. GPS = Global Positioning System; TEC = total electron content; CONUS = contiguous United States.

eventually dissipate every GW (Vadas, 2007). On 7 October, the background wind velocity is ~110 m/s in the southeast direction above altitude of ~300 km, meaning that the northward/westward propagating GWs have increased vertical wavelengths and can therefore propagate favorably to higher altitudes before dissipating from viscosity (e.g., Fritts & Vadas, 2008). The characteristics of the waves in the CTIDs are comparable to that of Super Typhoon Nepartak (2016, Chou, Lin, Yue, Chang, et al., 2017) and Super Typhoon Meranti (2016, Chou, Lin, Yue, Tsai, et al., 2017), which also suggests that the CTIDs are related to the CGWs induced by Hurricane Matthew.

## 5. Discussion

### 5.1. GW Propagation Coupling Between Different Layers

As we have shown through this analysis, multiple simultaneous observations from different sensors and instruments reveal a broad spectrum of CGWs associated with Hurricane Matthew at different altitude regions in the middle and upper atmosphere, which is unprecedented in the given configuration of sensors/instruments. The development and movement of a TC is steadier and longer lasting than a single thunderstorm (Azeem et al., 2015) or tornado (Nishioka et al., 2013). With multisatellite observations that cover different altitude ranges from the troposphere to the ionosphere, the GW coupling between different layers can be investigated in detail in order to study Hurricane Matthew.

AIRS observed GWs near Hurricane Matthew at 07:15 UTC on 1 October 2016 having a dominant horizontal wavelength of ~200 km at a height range of 30–40 km. At 06:51 UTC on 1 October 2016, VIIRS/DNB observed a set of GWs in the airglow layer (at an altitude of 85–90 km) to the northwest of Matthew having a horizontal wavelength of ~233 km, as well as shorter (24–27 km) horizontal wavelength GWs to the northeast of the storm. Due to its high/uniform resolution and the large swath coverage, the VIIRS/DNB also provided significant GW observations after 1 October 2016. Complementing the satellite imagery, GPS TEC observations on 1, 2, and 7 October over the CONUS also detected CTIDs/CGWs with horizontal wavelengths of ~340, ~270, and ~250 km, respectively.

Hoffmann et al. (2018) conduct a statistical analysis of TC-induced GWs that combines TCs' tracks and intensity estimates, AIRS GW data, and the stratospheric background winds. They find that the occurrence of GW peak events associated with the intensification of TCs is twice that of TC weakening. Further, the distribution of GW events with respect to TC intensity change (considering both of intensification and weakening) is significantly inclines toward increasing-intensity of TC's 10-min maximum sustained winds. Since TCs take place every year in almost every ocean and their life spans are much longer than a single convective cloud, observations at different stages of TCs can provide further evidence of the physical link between the TC intensity and GW production. For Hurricane Matthew, the period when the DNB collected approximately six images containing observable GWs (1–6 October 2016) nearly overlaps the time period when the storm's maximum sustained winds were greater than ~51.4 m/s (~100 kt), that is, its most intense phase of hurricane.

According to Yue et al. (2009), the mean background zonal wind is nearly zero just after the spring equinox and before the fall equinox in the stratosphere and lower mesosphere. This quiescence allows upward

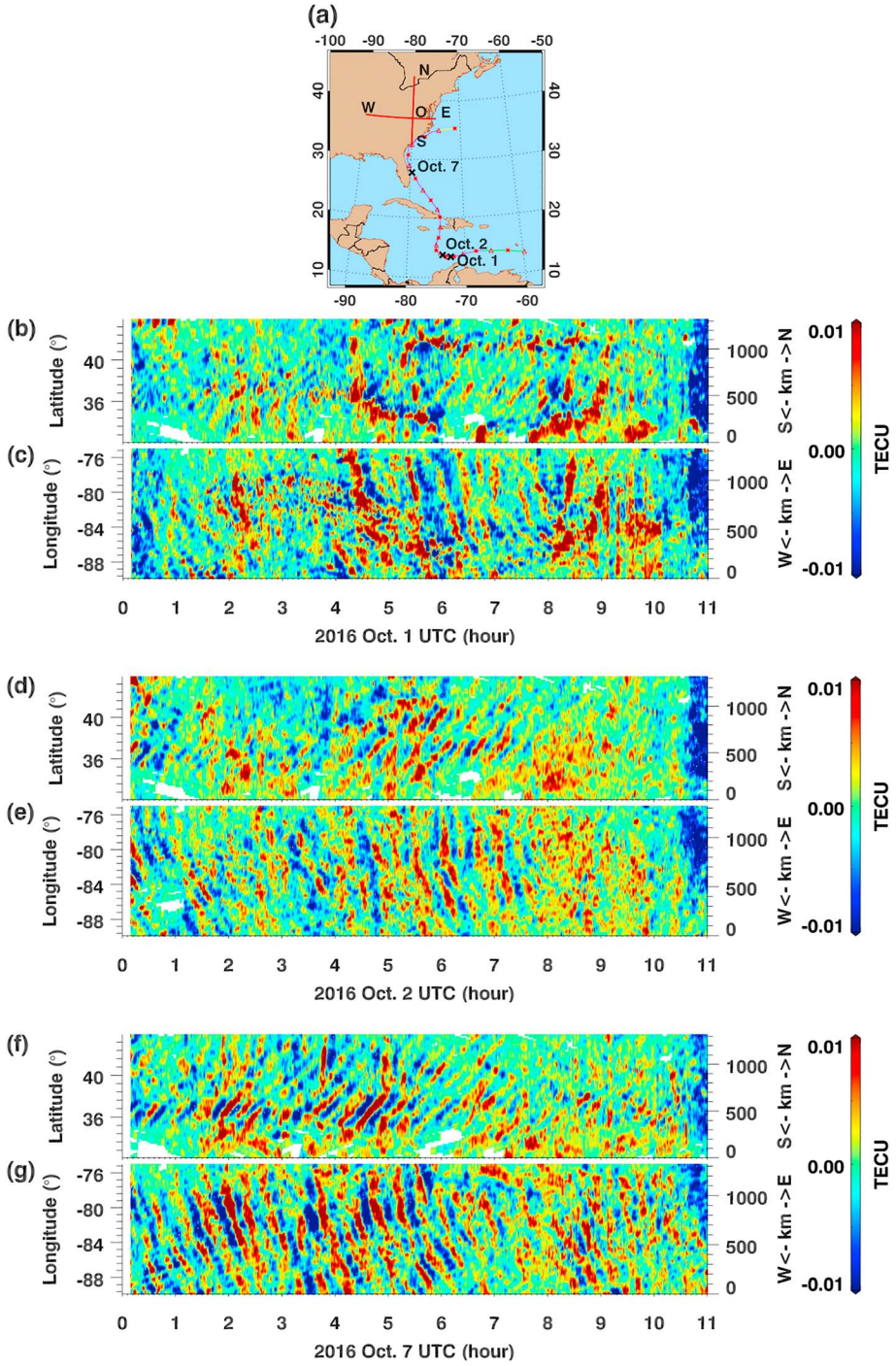


**Figure 9.** (a). Thumbnail map of hurricane trajectory (asterisks, triangles, and colored curves in the Atlantic Ocean). The locations of Hurricane Matthew at UTC 06:00 on 1, 2, and 7 October are shown as black crosses. Red lines in the eastern United States indicate the meridional and zonal orthogonal segments centered at (80°W, 37°N) that we use for analysis in Figures 9b–9h. The temporal slices of the GPS-TEC along the meridional and zonal red lines in Figure 9a are plotted as Figure 9b meridional keograms and (c) zonal keograms, respectively. Figures 9d and 9e, and 9g and 9h are the same as in Figures 9b and 9c, except on 2 October and 7 October 2016. GPS = Global Positioning System; TEC = total electron content.

propagating CGWs to reach the mesopause region without the concentric ring structure being distorted by intervening winds (Vadas et al., 2009). Similar background wind conditions may be the reason why the CGWs generated by Hurricane Matthew propagated into the mesosphere (and possibly the thermosphere)

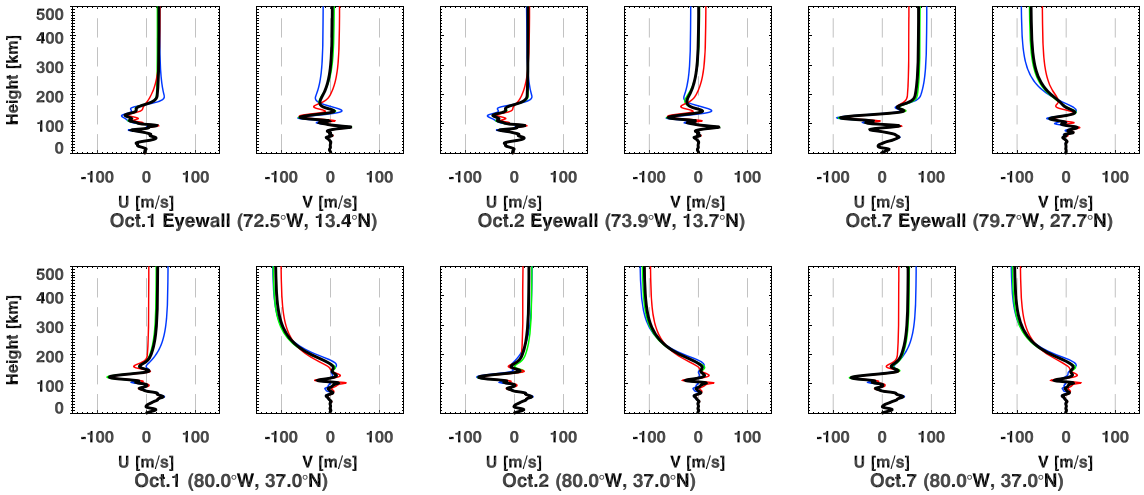


**Figure 10.** Upper panel, left to right: HWM14 zonal (U: left) and meridional (V: right) wind profiles at 05:00 (blue), 06:00 (green), 07:00 (red) UTC as well as the mean of these 3 times (black thick) over Hurricane Matthew on 1, 2, and 7 October 2016, respectively. Lower panel: Same as upper panel but at (80°W, 37°N) the intersection point O in Figure 9a.

with concentric ring structure remaining nearly intact over a large horizontal area. However, there are also many differences between the CGWs considered by Yue et al. (2009) and Hurricane Matthew. In Yue et al. (2009), the CGWs structures were associated with Colorado convection. These GWs had horizontal wavelengths of ~40–80 km and were associated with individual convective plumes/localized thunderstorms. In the case of Hurricane Matthew, the CGWs have much larger horizontal wavelengths and horizontal phase speeds, and therefore were most likely to have been generated by the overall updraft contribution from a large number of organized convective plumes within the complex system.

According to Kundu and Cohen (1990) and Yue et al. (2009), the intrinsic period $\tau_{Ir}$ of a GW can be expressed in terms of the horizontal radius $R$ of the convectively generated CGWs at the desired altitude $z$ as

$$\tau_{Ir} = \frac{2\pi}{N}\sec\alpha = \frac{2\pi}{N}\sqrt{1+\frac{R^2}{\Delta z^2}} \tag{1}$$

where $N = \sqrt{(g/\overline{\theta})d\overline{\theta}/dz}$ is Brunt-Väisälä (or buoyancy) frequency, $\Delta z$ is the vertical distance between the tropopause and atmospheric layer where the GW is observed, $\alpha$ is the angle between the vertical and the constant phase of the CGW at the horizontal radius $R$, which implies $\tan\alpha = R/\Delta z$. $\overline{\theta} = \overline{T}(p_0/\overline{p})^{R_d/C_p}$ is the potential temperature. $\overline{T}$ is the temperature, $\overline{p}$ is the air pressure, and $p_0 = \overline{p}(z=0)$, and $R_d = 287.058\ \mathrm{J\cdot K^{-1}\cdot kg^{-1}}$ is the gas constant for dry air. $C_p = 1005.0\ \mathrm{J\cdot K^{-1}\cdot kg^{-1}}$ is the specific heat at a constant pressure. $g$ is the gravitational acceleration. Equation (1) is derived under the assumptions that the background wind is constant, the background temperature is constant, the molecular viscosity is not (yet) important, and the Boussinesq assumption holds, that is, that $\lambda_z \ll 4\pi H$, where $\lambda_z$ is vertical wavelength and $H$ is scale height. Equation (1) explains why the period $\tau$ and horizontal wavelength $\lambda_H$ increase as the distance $R$ from the convective source increases.

Since equation (1) can be applicable for studies of convective storms (Azeem et al., 2015) and convective plumes in Vadas et al. (2009) and Yue et al. (2009) when these assumptions are met, we now input the characteristics of the GWs generated by Hurricane Matthew into equation (1) to see if it is applicable to Hurricane Matthew. Note from Figure 10 that the winds are relatively small below 90 km, and that they are less than the horizontal phase speeds of the CGWs in the thermosphere: thus, the first assumption is reasonably well satisfied, especially in the stratosphere and mesosphere. We assume that the GWs are excited at the tropopause at $z$~12 km, and the altitude of $F$ peak region is 310 km; hence $\Delta z = 310 - 12 = 308$ km. We calculate the average buoyancy period $2\pi/N$ along altitude $\Delta z$ from 12 to 310 km to be ~6.7 min at tropopause altitude using data from the Mass Spectrometer Incoherent Scatter (MSISE-00) model (Picone et al., 2002, see Figure 11a). The simple relation given by equation (1) is

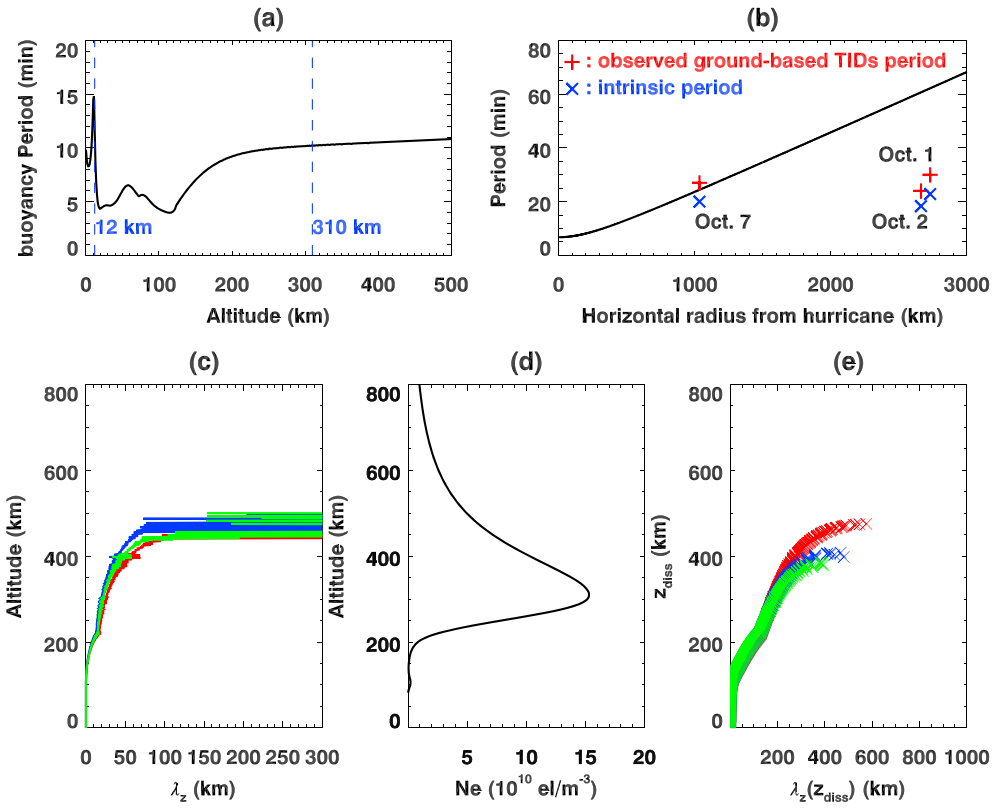


**Figure 11.** (a). The calculated Brunt-Väisälä (or buoyancy) period over the hurricane source region. (b) Observed periods (red crosses), intrinsic periods (blue crosses), and calculated intrinsic period $\tau_{Ir}$ with respect to horizontal distance from Hurricane Matthew (solid curve) using equation (1). (c). $\lambda_z$ along the altitude calculated by dispersion relationship equation (2). Red, blue, and green curves denote $k_H$ from TIDs data on 1, 2, and 7 October 2016, respectively. (see section 4.3) (d). The electron density at (35°N, 80°W) at time 06:00 UTC on 2 October 2016 data generated from the IRI model. (e) Vertical wavelengths $\lambda_z(z_{\text{diss}})$ as a function of $z_{\text{diss}}$ for all of the dissipating GWs with horizontal wave number $k_H$ from TIDs data on 1, 2, and 7 October, respectively (the same as in Figure 11b). IRI = International Reference Ionosphere; TIDs = traveling ionospheric disturbances; GWs = gravity waves.

plotted as a solid curve in Figure 11b. Using the HWM14 background wind shown in Figure 10, the intrinsic periods of the GPS-TIDs, $\tau_{Ir} = 2\pi/\omega_{Ir}$, are calculated from the observed ground-based periods $\tau_r = 2\pi/\omega_r$ using $\omega_{Ir} = \omega_r - kU - lV$ (e.g., equation 12 of Vadas, 2007). The results are shown as blue (intrinsic periods $\tau_{Ir}$) and red (ground-based periods $\tau_r$) crosses, respectively, in Figure 11b. According to the black curve in Figure 11b, the intrinsic period $\tau_{Ir}$ should be ~56 min at a distance ~2,500 km horizontally from the convective source at an altitude of 310 km. However, both $\tau_r$ and $\tau_{Ir}$ on 1 October (observed: ~30 min, intrinsic: ~29.5 min) and ~24 min on 2 October (observed: ~24 min, intrinsic: ~23.4 min) from the GPS-TIDs (see section 4.3 and Figure 11b) are much smaller than the intrinsic period estimate from equation (1). This is likely due to dissipative filtering of the GWs in the spectrum having large periods, since the GWs that propagate to the midthermospheric have intrinsic periods less than an hour (Vadas, 2007). Thus, the assumption that we made for equation 1, that we can neglect molecular viscosity, is not applicable in the *F* region.

We now analyze the observed TIDs using a GW dispersion relation that includes molecular viscosity and kinematic viscosity in the thermosphere. The buoyancy frequency is *N*, and the kinematic viscosity is represented as $\nu = \mu/\overline{\rho}$, in which $\overline{\rho}$ is from MSISE-00 and $\mu$ is the molecular viscosity. According to equation 53 in Vadas and Crowley (2017), $\mu = 3.34\times10^{-4}\overline{T}^{0.71}$ g·m$^{-1}$·s$^{-1}$ $(z \le z_\mu)$ and $\mu = \mu(z_\mu)\left(\frac{\overline{\rho}}{\overline{\rho}(z_\mu)}\right)^{\left(\frac{\beta}{3}\right)}$ $(z > z_\mu)$ with best fit values $z_\mu = 220$ km and $\beta = 2$, where $z_\mu$ is the altitude where $\mu$ begins to decrease. Although the

Prandtl number is $Pr$~0.6 in the thermosphere, we assume $Pr = 1$ in order to simplify the dispersion relation. Then, the GW dispersion relation is given by equation 58 of Vadas and Fritts (2005):

$$\left(\omega_{Ir} + \frac{m\nu}{H}\right)^2 = \frac{{k_H}^2 N^2}{{k_H}^2 + m^2 + \frac{1}{4H^2}} \tag{2}$$

where $m$ is the vertical wave number; $\omega_{Ir} = k_H(c_h - u_h)$ is intrinsic frequency; $k_H$ is the horizontal wave number; $c_h$ is the horizontal GW phase velocity; and $u_h$ is the horizontal wind speed along the GW propagation direction (which we take here from HWM14). The vertical wave number can be solved iteratively by a first guess for $m$ via setting $\nu = 0$ first in this equation.

Using the characteristics of the CTIDs observed in the GPS data at ~06:00 UTC on 1, 2, and 7 October 2016 and the HWM14 wind data at (80°W, 37°N), we calculate the vertical wave number $m$ as a function of altitude and show them in Figure 11c; the red, blue, green lines show the results on 1, 2, and 7 October 2016. As shown in the figure, the GWs dissipate at altitudes of ~400–450 km from molecular viscosity.

### 5.2. GWs Propagation Into the Thermosphere/Ionosphere Including Viscous Dissipation

With reference to European Incoherent Scatter Svalbard Radar statistics by Hocke et al. (1996), the electron density variation reached up to a time average of 5% of the background electron density at the altitude of ~210 km, and the variation was 3% at the altitude of ~225 km in the studies by Nicolls et al. (2014) at Puerto Rico. The former study likely did not include extremely strong convective sources, although the latter study may have included strong deep convection sources. In our study, the amplitudes of the TIDs are much smaller: the unsmoothed TID amplitudes from the convective storm event in 2014 was ±0.1 TECU (~1% of the background TEC, Azeem et al., 2015), and for the Hurricane Matthew event the amplitude was only ±0.05–0.07 TECU. One of the reasons why the TEC TID amplitudes might be so small here is that the $F$ region of ionosphere (where most of the TEC signal comes from) is quite thick. For example, the ion density of at 06:00 UTC on 2 October 2016, which is generated from the IRI model, is shown in Figure 11d. The width at half maximum of the ion density is ~200 km (the altitude of ~249–440 km). In the middle thermosphere, the TIDs induced by the GWs have $\lambda_z$ similar to that of the GWs (Nicolls et al., 2014). If the vertical wavelengths of the convectively generated GWs/TIDs are significantly smaller than the $F$ layer thickness, then the vertical integration of the electron density perturbations through the $F$ layer effectively *smooths out* the electron perturbations, thereby significantly decreasing the amplitudes of the resulting TEC TID perturbations. If $\lambda_z$ below hmF2 is much smaller than the full-width half-max of the $F$ layer (~200 km in this case), then TEC TID amplitudes are expected to be significantly smaller than the amplitudes of the TIDs.

Every upward propagating GW eventually dissipates in the thermosphere at a unique altitude given by its intrinsic parameters (Vadas, 2007). As a result, the electron density perturbations are negligible above the altitude where the GW dissipates. From Vadas (2007, equation 14), the vertical wave number at the altitude where a GW has its maximum momentum flux (and dissipates strongly above this altitude), $m_{\rm diss} = 2\pi/\lambda_z(z_{\rm diss})$, is:

$$m_{\rm diss} = \sqrt{\left(\frac{k_H N}{2H\nu}\right)^{2/5} {m_{\rm diss}}^{2/5} - k_H^2 - \frac{1}{4H^2}} \tag{3}$$

Here equation (3) is solved iteratively for the absolute value of $m_{\rm diss}$, as described in Vadas (2007). For GWs with horizontal wave numbers $k_H = \frac{2\pi}{340}\,{\rm km}^{-1}, \frac{2\pi}{270}\ {\rm km}^{-1}$ and $\frac{2\pi}{250}\ {\rm km}^{-1}$ (observed on 1, 2, and 7 October 2016, see section 4.3) but with a range of wave periods, we show $\lambda_z(z_{\rm diss})$ versus $z_{\rm diss}$ in red, blue, and green crosses in Figure 11e. The altitudes where $m_{\rm diss}$ levels off are typically near the altitudes where the highest-frequency GWs dissipate (Vadas, 2007). From Figure 11c, these particular GWs dissipate at altitudes of $z_{\rm diss} = 400 - 450$ km with $\lambda_z$~50 – 100 km. Note that $\lambda_z$ is smaller than the full-width half-max of the electron density profile from Figure 11d.

When a GW propagates through the ionosphere, it pushes and pulls plasma along the Earth's magnetic field lines via ion-neutral collisions. In the $F$ region, the ion velocity perturbation fluctuates with the same period as the GW and has the same horizontal and vertical wavelengths (Vadas & Nicolls, 2009). As the ions move

in response to these collisions, the electrons follow nearly simultaneously. Thus, the propagating GWs create propagating disturbances in the electron density. Such perturbations last as long as the GW exists—if the GW dissipates from molecular viscosity, then the TID also disappears because it is not a self-sustaining wave. Because the driver for the TID is the component of the GW's velocity vector along the direction of the magnetic field lines, the TID amplitude is maximum if the GW propagates along the magnetic field and is negligible if the GW propagates perpendicular to the magnetic field line (Vadas & Nicolls, 2009).

Equation A19 from Nicolls et al. (2014) can be used to estimate the amplitude of the electron density perturbations, $\delta N_{e0}/\overline{N_e}$, induced by a GW in the *F* region. This amplitude is proportional to the projection of the GW's velocity vector along the Earth's magnetic field line. At the east CONUS region (90–80°W, 35–45°N), the magnetic declination angle is ~10°W–0°, which is roughly parallel to the geographic longitude line. And the magnetic inclination there is ~60–70° downward, which is quite large. The tangent angle of these TIDs arcs at (35°N, 90°W) is approximately 30–45° from the 90°W geographic longitude line in the horizontal plane, as shown in Figure 9. Therefore, we can infer that the northwestward propagating CGWs have propagation directions that are approximately 25–40° from the magnetic field lines in the horizontal plane. Thus, a significant component of their perturbation velocity lies along the direction of the magnetic field, thereby ensuring that TIDs with significant amplitudes are created from these GWs. But because $\lambda_z$ is somewhat smaller than the full-width half-max of the electron density profile in Figure 11d, we do not expect the TEC perturbations to be very large in our case. This is likely why in our Hurricane Matthew case that the TEC perturbation amplitudes are only ±0.05–0.07 TECU. Although the amplitudes of these TEC perturbations are small, we can still determine their amplitudes from the large net of GPS receivers in the CONUS via data processing because of the short periods of these GWs.

## 6. Conclusions

This paper conducts a comprehensive evaluation of Hurricane Matthew, a system that prolifically generated GWs in October 2016 over the Caribbean Sea. It is worth noting that hurricane-generated GWs were observed in the stratosphere, mesosphere, and constantly in ionosphere. To our knowledge, this is the first comprehensive study of hurricane-generated GWs using multiple satellite data sets. The data used in this analysis were collected by AIRS on Aqua, VIIRS/DNB on Suomi NPP, and GPS TEC, which include both spaceborne and ground-based instruments.

From this analysis, we found that GWs are generated from deep convection associated with the hurricane over time periods of several hours, and that this occurred several times during the observations covering a week. These GWs were seen in the tropopause to the ionosphere with typical horizontal wavelengths of ~200–350 km. Although we do not know if the GWs observed at different heights were the same GWs, it is likely that the observed GWs are from the same overall source region. At ~07:15 UTC on 1 October 2016, AIRS observed concentric GWs with a horizontal wavelength of ~200 km at the altitude range of 30–40 km in the stratosphere. Just ~30 min before this AIRS observation, VIIRS/DNB observed both of the small-scale and large-scale concentric GWs with respective horizontal wavelengths of 28–30 km and ~233 km in the nightglow structures simultaneously.

On the following 6 days, similar GW patterns correlated with Hurricane Matthew's movement were also captured by DNB. Moreover, the DNB observation on 1 October is similar to Yue et al. (2014), which suggests that small-scale waves could be excited by a local TC eyewall and spiral rainbands latent heating mechanisms or overshooting, while the large-scale waves could be caused by the obstacle effect (whereby winds in the lower stratosphere move over the upper part of the hurricane cloud complex) or the mechanical oscillator effect. Lastly, over CONUS, the GWs that were excited by Hurricane Matthew were also detected in the TEC by GPS receivers. These TIDs have horizontal wavelengths of ~250–340 km and periods of ~20–30 min. Nearly all of the observed GWs/TIDs had concentric arc-ring structures, and their extrapolated centers were colocated with Hurricane Matthew on three different days.

Using the GW dispersion relationship and propagation theory provided by Vadas (2007), we analyzed the GPS-TID observations on 1, 2, and 7 October 2016 over the eastern United States. From the analysis, we inferred that the GWs propagated from the convective sources within Hurricane Matthew to an altitude of at most ~400–450 km. Above the altitude where a GWs dissipates, the amplitude of the associated TID is

negligible because a TID is not self-sustaining but must be maintained by an underlying propagating GW. The amplitudes of the TIDs induced by the GWs created by Hurricane Matthew (±0.05–0.07 TECU) are much smaller than other reported of TIDs induced by GWs (Hocke et al., 1996; Nicolls et al., 2014). This is partly because the GW propagation directions were not optimally aligned along the Earth's magnetic field lines. But it is mostly due to the smoothing effect caused by the vertical integration of the electron density over the bottom of ionosphere, since $\lambda_z$ is less than the full-width half-max of the electron density profile. This study therefore shows that extensive vertical coupling occurs over regions of deep convection from the troposphere all the way to the thermosphere and ionosphere via GWs. In order to increase our comprehensive understanding of the GW propagation throughout multiple regions of the atmosphere from deep convection, further model and/or GW specific observations will be performed.

**Acknowledgments**
Thanks to Mingjiao Jia for his many guidance and suggestions, Tong Dang's help on using HWM14, and Wen Yi's helpful discussion on data processing. Thanks to Erdal Yiğit for his helpful discussion with us. We thank our peer reviewers for the care and attention paid toward helping us improve the quality of this manuscript. S. X. and X. H. X. were supported by National Natural Science Foundation of China (41474129) and the Open Research Project of Large Research Infrastructures of CAS —*Study on the interaction between low-latitude/ midlatitude atmosphere and ionosphere based on the Chinese Meridian Project*. J. Y. was supported by NSF grant AGS-1834222. S. L. V. was supported by NSF grants AGS-1832988 and AGS-1552315. S. D. M. was supported by the NOAA JPSS Program Office. In section 1 (Introduction), the annual numbers of tropical cyclones during 1981–2016 are contributed by Chris Landsea and Sandy Delgado (https://www.aoml.noaa.gov/hrd/tcfaq/E10.html). The Extended Best-Track (EBT) data for North Atlantic TCs during 1988–2017 were downloaded from the Colorado State University (CSU) website (http://rammb.cira.colostate.edu/research/tropical_cyclones/tc_extended_best_track_dataset/). AIRS data were obtained from NASA Goddard Earth Sciences Data Information and Services Center. The AIRS GW data products used in this study can be obtained from the website at https://datapub.fz-juelich.de/slcs/airs/gravity_waves. The VIIRS Sensor Data Record data are distributed by the CIMSS Atmospheric Product and Evaluation and Test Elements (PEATE) and NOAA Comprehensive Large Array-data Stewardship System (CLASS). We acknowledge the use of publicly available ground-based GPS TEC data from the Southern California Integrated GPS Network, International GPS Service for Geodynamics, UNAVCO, Hartebeesthoek Radio Astronomy Observatory, Natural Resources Canada, Geoscience Australia, the Brazilian Institute of Geography and Statistics, University of New Brunswick, National Oceanic and Atmospheric Administration, and National Aeronautics and Space Administration.

## References

Alexander, M., Geller, M., McLandress, C., Polavarapu, S., Preusse, P., Sassi, F., et al. (2010). Recent developments in gravity-wave effects in climate models and the global distribution of gravity-wave momentum flux from observations and models. *Quarterly Journal of the Royal Meteorological Society*, *136*(650), 1103–1124.

Aumann, H. H., Chahine, M. T., Gautier, C., Goldberg, M. D., Kalnay, E., McMillin, L. M., et al. (2003). AIRS/AMSU/HSB on the aqua mission: Design, science objectives, data products, and processing systems. *IEEE Transactions on Geoscience and Remote Sensing*, *41*(2), 253–264. https://doi.org/10.1109/tgrs.2002.808356

Azeem, I., & Barlage, M. (2018). Atmosphere-ionosphere coupling from convectively generated gravity waves. *Advances in Space Research*, *61*(7), 1931–1941. https://doi.org/10.1016/j.asr.2017.09.029

Azeem, I., Vadas, S. L., Crowley, G., & Makela, J. J. (2017). Traveling ionospheric disturbances over the United States induced by gravity waves from the 2011 Tohoku tsunami and comparison with gravity wave dissipative theory. *Journal of Geophysical Research: Space Physics*, *122*, 3430–3447. https://doi.org/10.1002/2016JA023659

Azeem, I., Yue, J., Hoffmann, L., Miller, S. D., Straka, W. C., & Crowley, G. (2015). Multisensor profiling of a concentric gravity wave event propagating from the troposphere to the ionosphere. *Geophysical Research Letters*, *42*, 7874–7880. https://doi.org/10.1002/2015GL065903

Bauer, S. J. (1958). An apparent ionospheric response to the passage of hurricanes. *Journal of Geophysical Research*, *63*(1), 265–269. https://doi.org/10.1029/JZ063i001p00265

Bilitza, D., McKinnell, L.-A., Reinisch, B., & Fuller-Rowell, T. (2011). The International Reference Ionosphere today and in the future. *Journal of Geodesy*, *85*(12), 909–920. https://doi.org/10.1007/s00190-010-0427-x

Bishop, R. L., Aponte, N., Earle, G. D., Sulzer, M., Larsen, M. F., & Peng, G. S. (2006). Arecibo observations of ionospheric perturbations associated with the passage of Tropical Storm Odette. *Journal of Geophysical Research*, *111*, A11320. https://doi.org/10.1029/2006JA011668

Chane-Ming, F., Roff, G., Robert, L., & Leveau, J. (2002). Gravity wave characteristics over Tromelin Island during the passage of cyclone Hudah. *Geophysical Research Letters*, *29*(6), 1094. https://doi.org/10.1029/2001GL013286

Chou, M. Y., Lin, C. C. H., Yue, J., Chang, L. C., Tsai, H. F., & Chen, C. H. (2017). Medium-scale traveling ionospheric disturbances triggered by Super Typhoon Nepartak (2016). *Geophysical Research Letters*, *44*, 7569–7577. https://doi.org/10.1002/2017GL073961

Chou, M. Y., Lin, C. C. H., Yue, J., Tsai, H. F., Sun, Y. Y., Liu, J. Y., & Chen, C. H. (2017). Concentric traveling ionosphere disturbances triggered by Super Typhoon Meranti (2016). *Geophysical Research Letters*, *44*, 1219–1226. https://doi.org/10.1002/2016GL072205

Chun, H. Y., Goh, J. S., & Kim, Y. H. (2007). Characteristics of inertio-gravity waves revealed in rawinsonde data observed in Korea during 20 August to 5 September 2002. *Journal of Geophysical Research*, *112*, D16108. https://doi.org/10.1029/2006JD008348

Crowley, G., & Rodrigues, F. S. (2012). Characteristics of traveling ionospheric disturbances observed by the TIDDBIT sounder. *Radio Science*, *47*, RS0L22. https://doi.org/10.1029/2011RS004959

Demuth, J. L., DeMaria, M., & Knaff, J. A. (2006). Improvement of advanced microwave sounding unit tropical cyclone intensity and size estimation algorithms. *Journal of Applied Meteorology and Climatology*, *45*(11), 1573–1581. https://doi.org/10.1175/Jam2429.1

Dewan, E. M., Picard, R. H., O'Neil, R. R., Gardiner, H. A., Gibson, J., Mill, J. D., et al. (1998). MSX satellite observations of thunderstorm-generated gravity waves in mid-wave infrared images of the upper stratosphere. *Geophysical Research Letters*, *25*(7), 939–942. https://doi.org/10.1029/98GL00640

Dhaka, S. K., Takahashi, M., Shibagaki, Y., Yamanaka, M. D., & Fukao, S. (2003). Gravity wave generation in the lower stratosphere due to passage of the typhoon 9426 (Orchid) observed by the MU radar at Shigaraki (34.85 degrees N, 136.10 degrees E). *Journal of Geophysical Research*, *108*(D19), 4595. https://doi.org/10.1029/2003JD003489

Djuth, F. T., Sulzer, M. P., Elder, J. H., & Wickwar, V. B. (1997). High-resolution studies of atmosphere-ionosphere coupling at Arecibo Observatory, Puerto Rico. *Radio Science*, *32*(6), 2321–2344. https://doi.org/10.1029/97RS02797

Drob, D. P., Emmert, J. T., Meriwether, J. W., Makela, J. J., Doornbos, E., Conde, M., et al. (2015). An update to the Horizontal Wind Model (HWM): The quiet time thermosphere. *Earth and Space Science*, *2*, 301–319. https://doi.org/10.1002/2014EA000089

Espy, P. J., & Huppi, R. (1997). The intertropical convergence zone as a source of short-period mesospheric gravity waves near the equator. *Journal of Atmospheric and Solar - Terrestrial Physics*, *59*(13), 1665–1671. https://doi.org/10.1016/S1364-6826(96)00165-4

Fritts, D. C., & Alexander, M. J. (2003). Gravity wave dynamics and effects in the middle atmosphere. *Reviews of Geophysics*, *41*(1), 1003. https://doi.org/10.1029/2001rg000106

Fritts, D. C., & Vadas, S. L. (2008). Gravity wave penetration into the thermosphere: Sensitivity to solar cycle variations and mean winds. *Annales Geophysicae*, *26*(12), 3841–3861. https://doi.org/10.5194/angeo-26-3841-2008

Hines, C. O. (1960). Internal atmospheric gravity waves at ionospheric heights. *Canadian Journal of Physics*, *38*(11), 1441–1481.

Hocke, K., & Schlegel, K. (1996). A review of atmospheric gravity waves and travelling ionospheric disturbances: 1982-1995. *Annales Geophysicae-Atmospheres Hydrospheres and Space Sciences*, *14*(9), 917–940. https://doi.org/10.1007/s00585-996-0917-6

Hocke, K., Schlegel, K., & Kirchengast, G. (1996). Phases and amplitudes of TIDs in the high latitude *F* region observed by EISCAT. *Journal of Atmospheric and Terrestrial Physics*, *58*(1-4), 245–255. https://doi.org/10.1016/0021-9169(95)00033-x

Hoffmann, L., & Alexander, M. J. (2009). Retrieval of stratospheric temperatures from Atmospheric Infrared Sounder radiance measurements for gravity wave studies. *Journal of Geophysical Research*, *114*, D07105. https://doi.org/10.1029/2008JD011241

Hoffmann, L., & Alexander, M. J. (2010). Occurrence frequency of convective gravity waves during the North American thunderstorm season. *Journal of Geophysical Research*, *115*, D20111. https://doi.org/10.1029/2010JD014401

Hoffmann, L., Alexander, M. J., Clerbaux, C., Grimsdell, A. W., Meyer, C. I., Rossler, T., & Tournier, B. (2014). Intercomparison of stratospheric gravity wave observations with AIRS and IASI. *Atmospheric Measurement Techniques*, *7*(12), 4517–4537. https://doi.org/10.5194/amt-7-4517-2014

Hoffmann, L., Wu, X., & Alexander, M. J. (2018). Satellite observations of stratospheric gravity waves associated with the intensification of tropical cyclones. *Geophysical Research Letters*, *45*, 1692–1700. https://doi.org/10.1002/2017GL076123

Hoffmann, L., Xue, X., & Alexander, M. J. (2013). A global view of stratospheric gravity wave hotspots located with Atmospheric Infrared Sounder observations. *Journal of Geophysical Research: Atmospheres*, *118*, 416–434. https://doi.org/10.1029/2012JD018658

Holton, J. R. (1982). The role of gravity-wave induced drag and diffusion in the momentum budget of the mesosphere. *Journal of the Atmospheric Sciences*, *39*(4), 791–799. https://doi.org/10.1175/1520-0469(1982)039<0791:Trogwi>2.0.Co;2

Huang, A., Lu, G., Yue, J., Lyons, W., Lucena, F., Lyu, F., et al. (2018). Observations of red sprites above Hurricane Matthew. *Geophysical Research Letters*, *45*, 13,158–13,165. https://doi.org/10.1029/2018GL079576

Hung, R. J., & Kuo, J. P. (1978). Ionospheric observation of gravity-waves associated with Hurricane Eloise. *Journal of Geophysics-Zeitschrift Fur Geophysik*, *45*(1), 67–80.

Jin, S. G., Occhipinti, G., & Jin, R. (2015). GNSS ionospheric seismology: Recent observation evidences and characteristics. *Earth-Science Reviews*, *147*, 54–64. https://doi.org/10.1016/j.earscirev.2015.05.003

Kaplan, E., & Hegarty, C. (2005). *Understanding GPS: Principles and applications*. Norwood, MA: Artech house.

Kim, S. Y., & Chun, H. Y. (2010). Stratospheric gravity waves generated by Typhoon Saomai (2006). Numerical modeling in a moving frame following the typhoon. *Journal of the Atmospheric Sciences*, *67*(11), 3617–3636. https://doi.org/10.1175/2010JAS3374.1

Kim, S. Y., Chun, H. Y., & Wu, D. L. (2009). A study on stratospheric gravity waves generated by Typhoon Ewiniar: Numerical simulations and satellite observations. *Journal of Geophysical Research*, *114*, D22104. https://doi.org/10.1029/2009JD011971

Kuester, M. A., Alexander, M. J., & Ray, E. A. (2008). A model study of gravity waves over Hurricane Humberto (2001). *Journal of the Atmospheric Sciences*, *65*(10), 3231–3246. https://doi.org/10.1175/2008jas2372.1

Kundu, P., & Cohen, L. (1990). *Fluid mechanics*, (p. 638). Calif: Academic.

Lai, C., Yue, J., Xu, J. Y., Straka, W. C., Miller, S. D., & Liu, X. (2017). Suomi NPP VIIRS/DNB imagery of nightglow gravity waves from various sources over China. *Advances in Space Research*, *59*(8), 1951–1961. https://doi.org/10.1016/j.asr.2017.01.041

Lee, T. E., Miller, S. D., Turk, F. J., Schueler, C., Julian, R., Deyo, S., et al. (2006). The NPOESS VIIRS day/night visible sensor. *Bulletin of the American Meteorological Society*, *87*(2), 191–199. https://doi.org/10.1175/Bams-87-2-191

Lindzen, R. S. (1981). Turbulence and stress owing to gravity-wave and tidal breakdown. *Journal of Geophysical Research*, *86*(Nc10), 9707–9714. https://doi.org/10.1029/JC086iC10p09707

Lomb, N. R. (1976). Least-squares frequency-analysis of unequally spaced data. *Astrophysics and Space Science*, *39*(2), 447–462. https://doi.org/10.1007/Bf00648343

Miller, S. D., Mills, S. P., Elvidge, C. D., Lindsey, D. T., Lee, T. F., & Hawkins, J. D. (2012). Suomi satellite brings to light a unique frontier of nighttime environmental sensing capabilities. *Proceedings of the National Academy of Sciences of the United States of America*, *109*(39), 15,706–15,711. https://doi.org/10.1073/pnas.1207034109

Miller, S. D., Straka, W., Mills, S. P., Elvidge, C. D., Lee, T. F., Solbrig, J., et al. (2013). Illuminating the capabilities of the Suomi National Polar-Orbiting Partnership (NPP) Visible Infrared Imaging Radiometer Suite (VIIRS) day/night band. *Remote Sensing*, *5*(12), 6717–6766. https://doi.org/10.3390/rs5126717

Miller, S. D., Straka, W. C., Yue, J., Seaman, C. J., Xu, S., Elvidge, C. D., et al. (2018). The dark side of Hurricane Matthew: Unique perspectives from the VIIRS day/night band. *Bulletin of the American Meteorological Society*. https://doi.org/10.1175/bams-d-17-0097.1

Miller, S. D., Straka, W. C. 3rd, Yue, J., Smith, S. M., Alexander, M. J., Hoffmann, L., et al. (2015). Upper atmospheric gravity wave details revealed in nightglow satellite imagery. *Proceedings of the National Academy of Sciences of the United States of America*, *112*(49), E6728–E6735. https://doi.org/10.1073/pnas.1508084112

Nicolls, M. J., Vadas, S. L., Aponte, N., & Sulzer, M. P. (2014). Horizontal parameters of daytime thermospheric gravity waves and *E* region neutral winds over Puerto Rico. *Journal of Geophysical Research: Space Physics*, *119*, 575–600. https://doi.org/10.1002/2013JA018988

Nishioka, M., Tsugawa, T., Kubota, M., & Ishii, M. (2013). Concentric waves and short-period oscillations observed in the ionosphere after the 2013 Moore EF5 tornado. *Geophysical Research Letters*, *40*, 5581–5586. https://doi.org/10.1002/2013GL057963

Perwitasari, S., Sakanoi, T., Yamazaki, A., Otsuka, Y., Hozumi, Y., Akiya, Y., et al. (2015). Coordinated airglow observations between IMAP/VISI and a ground-based all-sky imager on concentric gravity wave in the mesopause. *Journal of Geophysical Research: Space Physics*, *120*, 9706–9721. https://doi.org/10.1002/2015JA021424

Pfister, L., Chan, K. R., Bui, T. P., Bowen, S., Legg, M., Gary, B., et al. (1993). Gravity-waves generated by a tropical cyclone during the step tropical field program—A case-study. *Journal of Geophysical Research*, *98*, 8611–8638. https://doi.org/10.1029/92JD01679

Picone, J. M., Hedin, A. E., Drob, D. P., & Aikin, A. C. (2002). NRLMSISE-00 empirical model of the atmosphere: Statistical comparisons and scientific issues. *Journal of Geophysical Research*, *107*(A12), 1468. https://doi.org/10.1029/2002JA009430

Sato, K. (1993). Small-scale wind disturbances observed by the Mu radar during the passage of Typhoon Kelly. *Journal of the Atmospheric Sciences*, *50*(4), 518–537. https://doi.org/10.1175/1520-0469(1993)050<0518:Sswdob>2.0.Co;2

Scargle, J. D. (1982). Studies in astronomical time series analysis. II-Statistical aspects of spectral analysis of unevenly spaced data. *The Astrophysical Journal*, *263*, 835–853.

Seaman, C. J., & Miller, S. D. (2013). VIIRS captures aurora motions. *Bulletin of the American Meteorological Society*, *94*(10), 1491–1493.

Song, Q., Ding, F., Zhang, X. X., & Mao, T. (2017). GPS detection of the ionospheric disturbances over China due to impacts of Typhoons Rammasum and Matmo. *Journal of Geophysical Research: Space Physics*, *122*, 1055–1063. https://doi.org/10.1002/2016JA023449

Stewart, S. R. (2017). National hurricane center tropical cyclone report: Hurricane Matthew (AL142016)*Rep*., 96 pp.

Suzuki, S., Vadas, S., Shiokawa, K., Otsuka, Y., Kawamura, S., & Murayama, Y. (2013). Typhoon-induced concentric airglow structures in the mesopause region. *Geophysical Research Letters*, *40*, 5983–5987. https://doi.org/10.1002/2013GL058087

Taylor, M. J., & Hapgood, M. A. (1988). Identification of a thunderstorm as a source of short period gravity waves in the upper atmospheric nightglow emissions. *Planetary and Space Science*, *36*(10), 975–985. https://doi.org/10.1016/0032-0633(88)90035-9

Trishchenko, A. P., & Garand, L. (2012). Observing polar regions from space: Advantages of a satellite system on a highly elliptical orbit versus a constellation of low Earth polar orbiters. *Canadian Journal of Remote Sensing*, *38*(1), 12–24. https://doi.org/10.5589/m12-009

Vadas, S. L. (2007). Horizontal and vertical propagation and dissipation of gravity waves in the thermosphere from lower atmospheric and thermospheric sources. *Journal of Geophysical Research*, *112*, A06305. https://doi.org/10.1029/2006JA011845

Vadas, S. L., & Becker, E. (2018). Numerical modeling of the excitation, propagation, and dissipation of primary and secondary gravity waves during wintertime at McMurdo station in the Antarctic. *Journal of Geophysical Research: Atmospheres*, *123*, 9326–9369. https://doi.org/10.1029/2017JD027974

Vadas, S. L., & Crowley, G. (2010). Sources of the traveling ionospheric disturbances observed by the ionospheric TIDDBIT sounder near Wallops Island on 30 October 2007. *Journal of Geophysical Research*, *115*, A07324. https://doi.org/10.1029/2009JA015053

Vadas, S. L., & Crowley, G. (2017). Neutral wind and density perturbations in the thermosphere created by gravity waves observed by the TIDDBIT sounder. *Journal of Geophysical Research: Space Physics*, *122*, 6652–6678. https://doi.org/10.1002/2016JA023828

Vadas, S. L., & Fritts, D. C. (2005). Thermospheric responses to gravity waves: Influences of increasing viscosity and thermal diffusivity. *Journal of Geophysical Research*, *110*, D15103. https://doi.org/10.1029/2004JD005574

Vadas, S. L., & Liu, H. L. (2009). Generation of large-scale gravity waves and neutral winds in the thermosphere from the dissipation of convectively generated gravity waves. *Journal of Geophysical Research*, *114*, A10310. https://doi.org/10.1029/2009JA014108

Vadas, S. L., & Liu, H. L. (2013). Numerical modeling of the large-scale neutral and plasma responses to the body forces created by the dissipation of gravity waves from 6 h of deep convection in Brazil. *Journal of Geophysical Research: Space Physics*, *118*, 2593–2617. https://doi.org/10.1002/jgra.50249

Vadas, S. L., Liu, H. L., & Lieberman, R. S. (2014). Numerical modeling of the global changes to the thermosphere and ionosphere from the dissipation of gravity waves from deep convection. *Journal of Geophysical Research: Space Physics*, *119*, 7762–7793. https://doi.org/10.1002/2014JA020280

Vadas, S. L., & Nicolls, M. J. (2009). Temporal evolution of neutral, thermospheric winds and plasma response using PFISR measurements of gravity waves. *Journal of Atmospheric and Solar - Terrestrial Physics*, *71*(6-7), 744–770. https://doi.org/10.1016/j.jastp.2009.01.011

Vadas, S. L., Yue, J., She, C. Y., Stamus, P. A., & Liu, A. Z. (2009). A model study of the effects of winds on concentric rings of gravity waves from a convective plume near Fort Collins on 11 May 2004. *Journal of Geophysical Research*, *114*, D06103. https://doi.org/10.1029/2008JD010753

Wu, J., Xue, X., Hoffmann, L., Dou, X., Li, H., & Chen, T. (2015). A case study of typhoon-induced gravity waves and the orographic impacts related to Typhoon Mindulle (2004) over Taiwan. *Journal of Geophysical Research: Atmospheres*, *120*, 9193–9207. https://doi.org/10.1002/2015JD023517

Yue, J., Hoffmann, L., & Joan Alexander, M. (2013). Simultaneous observations of convective gravity waves from a ground-based airglow imager and the AIRS satellite experiment. *Journal of Geophysical Research: Atmospheres*, *118*, 3178–3191. https://doi.org/10.1002/jgrd.50341

Yue, J., Miller, S. D., Hoffmann, L., & Straka, W. C. (2014). Stratospheric and mesospheric concentric gravity waves over tropical cyclone Mahasen: Joint AIRS and VIIRS satellite observations. *Journal of Atmospheric and Solar - Terrestrial Physics*, *119*, 83–90. https://doi.org/10.1016/j.jastp.2014.07.003

Yue, J., Vadas, S. L., She, C.-Y., Nakamura, T., Reising, S. C., Liu, H.-L., et al. (2009). Concentric gravity waves in the mesosphere generated by deep convective plumes in the lower atmosphere near Fort Collins, Colorado. *Journal of Geophysical Research*, *114*, D06104. https://doi.org/10.1029/2008JD011244